



## DIPLOMARBEIT

# **Experimental Setup NIELS for Energy Loss Measurement of Slow Highly Charged Ions based on Time-of-Flight**

Ausgeführt am Institut für  
Angewandte Physik  
der Technischen Universität Wien  
Wiedner Hauptstraße 8-10 / 134  
1040 Wien  
der Technischen Universität Wien

unter der Anleitung von

Dr.rer.nat. Richard Arthur WILHELM  
Univ.-Prof. Dr. Friedrich AUMAYR

durch

DAVID MELINC  
Matrikelnummer 1125165  
Zimmermannplatz 4/31  
1090 Wien

---

Datum

---

David Melinc



# Abstract

The unique electronic properties of ultimately thin materials like single layer graphene (SLG) or carbon nanomembranes (CNM) have attracted enormous attention as excellent candidates for future nanoelectronics. Disorder, as caused e.g. by collisions with high energetic electrons or ions, alter the electronic structure and therefore allow to modify and tailor the properties of these 2D material. Collision studies between ions and freestanding SLG are also of fundamental interest, because they bridge the gap between atomic collisions in gaseous and those in solid targets [1]. To learn more about the microscopic interaction mechanism we built the new experimental setup NIELS (Neutral and Ion Energy Loss Spectrometry) based on the time-of-flight (TOF) technique. In addition to the TOF a Vienna electron statistics detector will be mounted [2], which enables us to combine these two methods and do coincidence measurements of electron emission, energy loss and charge exchange associated with highly charged ion impact on 2D materials simultaneously.

A room-temperature electron beam ion source (Dreebit EBIS-A), which is equipped with a Wien filter and mounted on a high voltage platform, provides highly charged ions of different charge states  $Q$  at kinetic energies ranging from  $100\text{eV}\times Q$  to  $12\text{keV}\times Q$ . With this setup we achieve an energy resolution of  $\frac{\Delta E}{E} < 2\%$ , which is sufficient to measure charge state enhanced kinetic energy loss [1] and aim on measure not only energy loss for charged and neutral transmitted ions/atoms due to interaction processes with conductors like SLG but also with insulators like boron nitride and CNM or semiconductor like molybdenum disulfide.

In this thesis the design, installation and calibration of the NIELS setup will be described. First measurements performed with 1nm thick carbon nanomembranes as well as freestanding single layer graphene are presented in chapter 3.

# Kurzfassung

Die einzigartigen Eigenschaften von leitenden 2D-Materialien wie single-layer-graphene (SLG) oder Kohlenstoff Nanomembranen (CNM) haben seit deren Entdeckung viel Aufmerksamkeit, als ausgezeichnete Kandidaten für zukünftige Anwendungen in der Nanoelektronik, auf sich gezogen. Bewusste Störung der Gitter- und Elektronenstruktur beispielsweise durch Kollisionen mit Elektronen oder hochgeladenen Ionen erlauben es die Eigenschaften eben dieser Materialien maßgeschneidert zu verändern.

Stoßprozesse zwischen freistehendem SLG und Ionen sind außerdem von fundamentalem Interesse, da diese das Bindeglied zwischen atomaren Stoßprozessen in Gasen und festen Targets bilden [1]. Um mehr über diese mikroskopischen Wechselwirkungsprozesse zu erfahren wurde das Experiment NIELS (Neutral and Ions Energy Loss Spectrometry) gebaut.

NIELS basiert auf dem Prinzip der Flugzeitspektrometrie (TOF-Spektroskopie). Neben der TOF-Spektroskopie verfügt NIELS auch über einen Elektronenstatistikdetektor [2] weswegen mit NIELS Koinzidenzmessungen von Energieverlust, Ladungsaustausch und Elektronenemission möglich sind.

Eine Elektronenstrahlionenquelle (Dreerbit EBIS-A) versorgt den Versuchsaufbau mit hochgeladenen Ionen verschiedener Ladungszustände mit kinetischen Energien von  $100\text{eV} \times Q$  bis zu  $12\text{keV} \times Q$ . Des Weiteren ist die Quelle mit einem Wienfilter ausgestattet, welcher die Auswahl des Anfangsladungszustandes erlaubt und ist auf einer Hochspannungsplattform angebracht, wodurch die kinetische Energie der austretenden Ionen eingestellt werden kann. Mit diesem Experiment erreichen wir eine Energieauflösung von  $\frac{\Delta E}{E} < 2\%$  was ausreichend ist um ladungszustandsensible kinetische Energieverluste messen zu können. Des Weiteren ist es geplant nicht nur den Energieverlust von geladenen und neutralen Ionen nach Wechselwirkungen mit elektrisch leitenden Materialien zu beobachten, sondern auch mit Isolatoren wie hexagonales Bornitrid (hBn) oder Halbleitern wie Molybdän(IV)-sulfid ( $\text{MoS}_2$ ).

In der vorliegenden Arbeit wird das Design, die Installation und die Kalibrierung von NIELS beschrieben. Erste Messungen mit 1nm dicke Kohlenstoff Nanomembranen und freistehendem einlagigem Graphen werden in Kapitel 3 präsentiert.



# CONTENTS

<b>1. INTRODUCTION.....</b>	<b>5</b>
<b>A. MOTIVATION.....</b>	<b>5</b>
<b>B. STATE OF THE ART.....</b>	<b>5</b>
<b>C. AIM OF THIS THESIS.....</b>	<b>10</b>
<b>2 EXPERIMENTAL SETUP.....</b>	<b>11</b>
<b>A. ION SOURCE.....</b>	<b>12</b>
I) WORKING PRINCIPLE.....	12
II) IMPORTANT PARAMETERS OF THE EBIS-A.....	14
a) Beam diameter.....	14
b) Source parameter - (U0-Ub-Udeaccelaration) validation through TOF with deceleration voltages.....	14
c) Charge-state-spectrum.....	15
<b>B. TIME OF FLIGHT (TOF).....</b>	<b>16</b>
I) PRINCIPLE OF THE TOF –SPECTROSCOPY.....	17
II) RESOLUTION OF THE SPECTROMETER.....	17
III) PRODUCTION OF A START SIGNAL.....	18
a) Mechanical beam chopper.....	18
b) Electrostatic beam chopper.....	20
c) Pulsing the particle source.....	24
d) Using the electron emission statistics as start signal.....	24
IV) IMPORTANT PARAMETERS FOR THE TOF-SPECTROSCOPY.....	26
a) Distance between chopper and target.....	26
b) Distance between chopper and MCP.....	26
c) Chopper voltage.....	27
d) Chopper signal passage of time.....	27
e) Timing resolution of the TOF-spectroscopy.....	29
<b>C. COLLIMATOR.....</b>	<b>32</b>
<b>D. TARGET HOLDER.....</b>	<b>32</b>
<b>E. MCP.....</b>	<b>33</b>
<b>F. Q-BLANKER.....</b>	<b>34</b>
I) RELATION BETWEEN Q-BLANKER DEFLECTION VOLTAGE AND DEVIATION ON THE MCP.....	34
<b>3 RESULTS AND DISCUSSION.....</b>	<b>37</b>
<b>A. TOF-SPECTROSCOPY.....</b>	<b>37</b>
<b>B. TOF-SPECTRUM WITH POOR CHOPPER SETTINGS.....</b>	<b>38</b>
<b>C. CHARGE STATE SPECTRUM OF CNM AND GRAPHEN TARGET.....</b>	<b>39</b>
<b>4 CONCLUSION AND OUTLOOK.....</b>	<b>41</b>
<b>A. EVALUATION CONCEPT.....</b>	<b>41</b>
<b>B. INSTALLATION AND START OF ELECTRON EMISSION STATISTICS.....</b>	<b>42</b>
<b>C. ADJUSTMENT Q-BLANKER.....</b>	<b>42</b>
<b>D. REPLACEMENT OF THE COOLING CYCLE.....</b>	<b>42</b>
<b>E. SIMPLIFICATION OF TARGET EXCHANGE.....</b>	<b>43</b>



# 1. Introduction

## **A. Motivation**

The interaction of highly charged ions (HCI) with solid surfaces has been a much-researched topic in the last two decades due to the wide range of possible applications [2-7,9-23]. HCI are of particular interest due to their high potential energy.

When interacting with a solid, HCI deposit their potential energy in a small area of a few tens of square nanometers in a very short time (10 fs). Due to the large number of emitted secondary particles (electrons), electron emission statistics can help to improve the understanding of interaction processes between charged projectiles and matter. 2D materials, e.g. single layer graphene (SLG) [8] are so thin that the distance travelled by an ion through the solid is too short to get in an equilibrium state, which is characterized by a (short time-averaged) constant charge state. Therefore, they are offering a great possibility to investigate energy deposition linked with non equilibrium charge states. With the access to this extraordinary material, interaction studies between highly charged ions and freestanding SLG become of genuine interest, because they bridge the gap between atomic collisions in gaseous and those in solid targets [1].

## **B. State of the art**

Over the last few decades the interaction of particles carrying both kinetic and potential energy with solid matter inspired an immense amount of experimental as well as theoretical research [2-7,9-23]. J. Burgdörfer et al. described neutralization of highly charged projectiles above metal surfaces successfully in the framework of a “classical over-the-barrier” model [9]. When these ions reach a critical distance from a surface the strong attractive potential of the latter accelerates electrons towards the HCI and, approximately, half of them end up captured into highly excited states, forming “hollow atoms” [12]. When the ion reaches the surface electrons in states with radii in excess of a characteristic surface screening length are “peeled off” [9,10] or form simultaneously a more compact screening cloud around the projectile, which is in principle a smaller, hollow atom inside the solid.

To probe interaction processes in very thin target materials (2D materials) slow HCI are ideal tools due to their energy deposition confinement to shallow surface regions.

E. Gruber reviewed most recently measurements regarding the short-time response of ultimate thin single layer graphene due to the irradiation with HCI ( $\text{Xe}^{35+}$ ), which results in an extremely large, local external field: the Coulomb field of an approaching HCI [24]. Time-dependent density functional theory (TDDFT) calculations of interactions between Xenon and graphene reveal that large numbers of electrons are extracted from a very small surface area of graphene, which implies a high local surface current density of the solid. Depending on the initial charge state the HCI captures and stabilizes between 20 and 30 electrons during its transmission through a 2D material. The actual number of captured electrons, without being reemitted due to autoionization processes as function of interaction time, is shown in fig. 1.1.

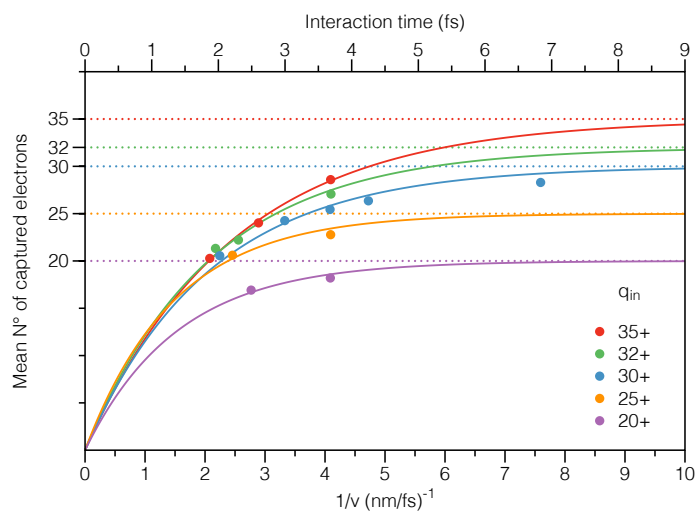


**Figure 1.1: Average number of captured and stabilized electrons after transmission of highly charged Xenon through SLG as a function of the invers projectile velocity for different incident charge states. Taken from [24]**

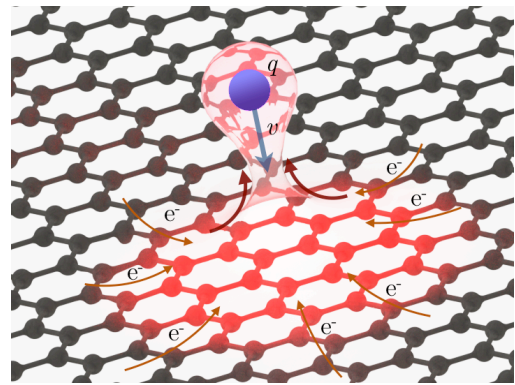


**Figure 1.2: Principle of the interaction process between SLG and an oncoming highly charged ion (HCI). The HCI extracts tens of electrons from a very narrow area within femtoseconds leading to a temporary charge-up of the impact region. Taken from [24]**

The TDDFT study illustrates both that the charge is extracted from the area of graphene with radius  $R=5 \text{ \AA}$  around the impact point, which consequently can be defined as an interaction region (fig. 1.2), and that the electron flow along the graphene layer compensates the electron extraction by the HCI on the timescale of the collision (fs). Otherwise the absorbed energy on a timescale small compared with lattice vibrations would result in Coulomb explosion tearing large holes (of the order of 10 nm) into the SLG, as was observed for carbon nanomembranes [25,26].

As neutralization is incomplete, charge state dependent effects on the energy loss can be observed. The energy loss, as experimentally deduced from the positions of the peaks for exit charge states  $q_{out}=2$  and  $q_{out}=4$ , increases quadratic with the incident charge state (figures 1.3,1.4).

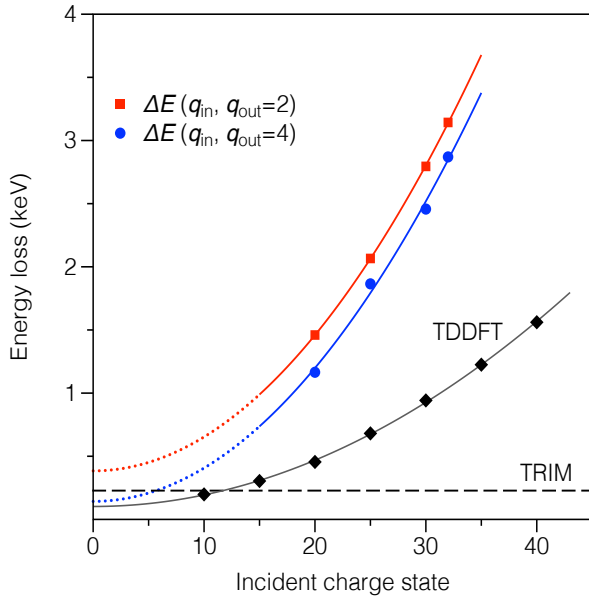


**Figure 1.3: Experimentally determined behavior of energy loss measurements for ions passing SLG with exit charge state  $q_{out}=2$  and  $q_{out}=4$  as a function of the incident charge state  $q_{in}$ . The kinetic energy for all projectiles was 40 keV. The dashed line shows the result from a TRIM simulation for a graphite layer of 3 Å thickness and results from TDDFT calculations, which reproduce the parabolic dependence and the order of magnitude of the energy loss are compared with experimental data points that are fitted by a quadratic function. Taken from [24]**

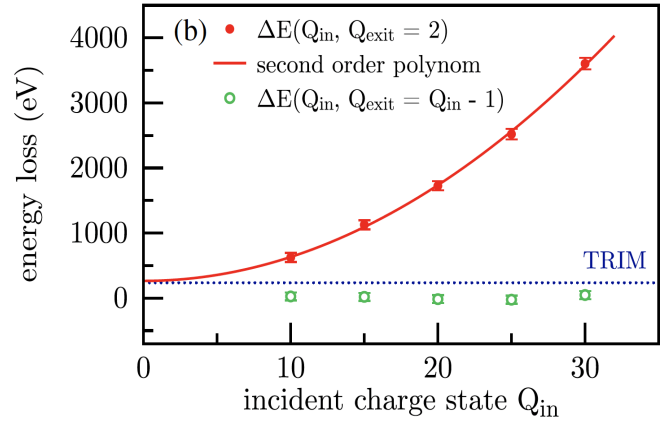


**Figure 1.4: The energy loss is shown for interactions between CNM and Xenon ions with exit charge state  $Q_{exit} = 2$  (red) and for ions with a charge loss of  $\Delta Q = 1$  (green) (maximum and minimum  $\Delta Q$ ). The experimental data was fitted by a second order polynomial. The dotted lines show the equilibrium charge and the result from a standard TRIM simulation, respectively. Taken from [1]**

Investigations with transmission electron microscopy (TEM) (fig. 1.5) or scanning transmission electron microscopy (STEM) do not show any localized defects in freestanding single layer graphene [27]. The absence of any traces of large-scale lattice deformations thus confirms the intrinsic ability of suspended SLG to locally sustain exceptionally high current densities, even though it cannot efficiently diffuse heat to a substrate [28,29]. Hence SLG provides tens of electrons for charge neutralization of a single slow highly charged ion in the space of a few femtoseconds, without any traces of fatigue [24].

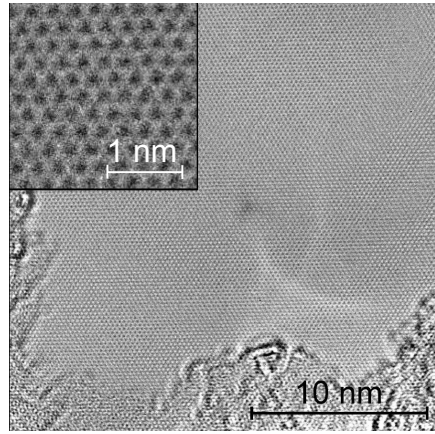


**Figure 1.5:** TEM image of a freestanding monolayer of graphene after irradiation with  $\text{Xe}^{40+}$  ions at 180 keV with an applied fluence of  $10^{12}$  ions per  $\text{cm}^2$  (about six impacts on the shown scale). No holes or nanosized topographic defects could be observed. The inset shows the intact hexagonal structure of the graphene sample. Taken from [24]

Due to the amount of transferred charge additional information about the interactions can be revealed. While a typical transmission spectrum of slow highly charged Xenon through SLG (fig. 1.6) shows a distribution of different exit charge states, with a mean value  $q_{\text{out}}$  shifted towards smaller exit charge states for slower ions, the spectra of Xenon through carbon nanomembranes (CNM) (fig. 1.7) on the other hand shows two distinct exit charge state distributions accompanied by charge exchange dependent kinetic energy losses, indicating that a 1 nm carbon layer is thin enough to address pre-equilibrium interaction processes of ions in solids [1]. In both cases even for the smallest velocities (largest interaction times)  $q_{\text{out}}$  stays significantly larger than the equilibrium charge state of a Xenon ion in a solid target ( $q_{\text{eq}} = 1$ ) [30]. The energy loss measurements for ions sustaining large charge loss show a quadratic dependency on the incident charge state, indicating that equilibrium stopping force values cannot be applied in this case. For carbon foils with larger thicknesses of 5 and 10 nm Schenkel *et al.* found evidence for a charge state dependent stopping force [31]. Schenkels measurements showed for the first time the presence of strong preequilibrium contributions to the energy loss of slow, heavy ions in solids. Wilhelm *et al.* concluded that charge state enhanced elastic scattering potential may play a major role for the increase in energy loss rather than charge state enhanced inelastic losses [1]. Therefore, the interaction experiments of HCl and 2D materials connect scattering experiments of ions on gaseous and on solid targets. The fact that the measured projectile energy loss can be assigned to the electronic excitations approves results obtained in studies for low projectile charges [32], therefore this clarification provides a consistent link between charge transfer and energy loss processes and allows explaining the absence of the induced damage despite the large energy deposition.

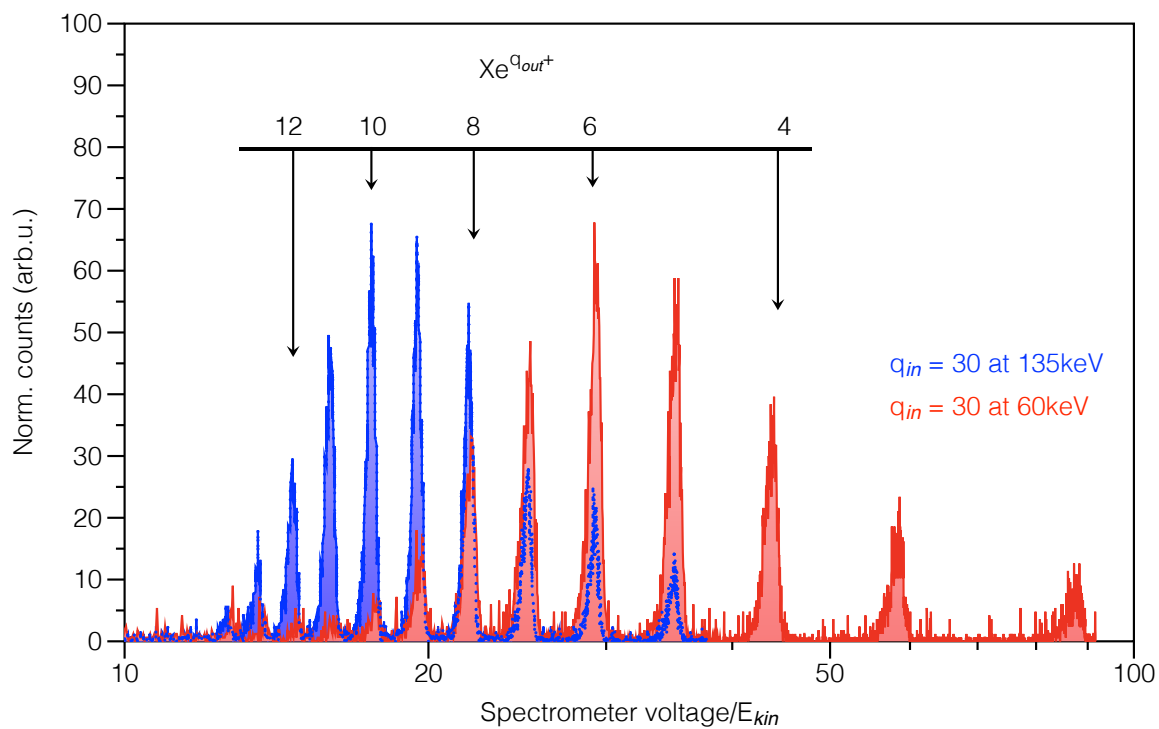


Figure 1.6: Typical transmission spectra of a  $\text{Xe}^{30+}$  beam at kinetic energies of 135 and 60 keV (blue and red, respectively transmitted through a freestanding SLG sheet. Taken from [24]

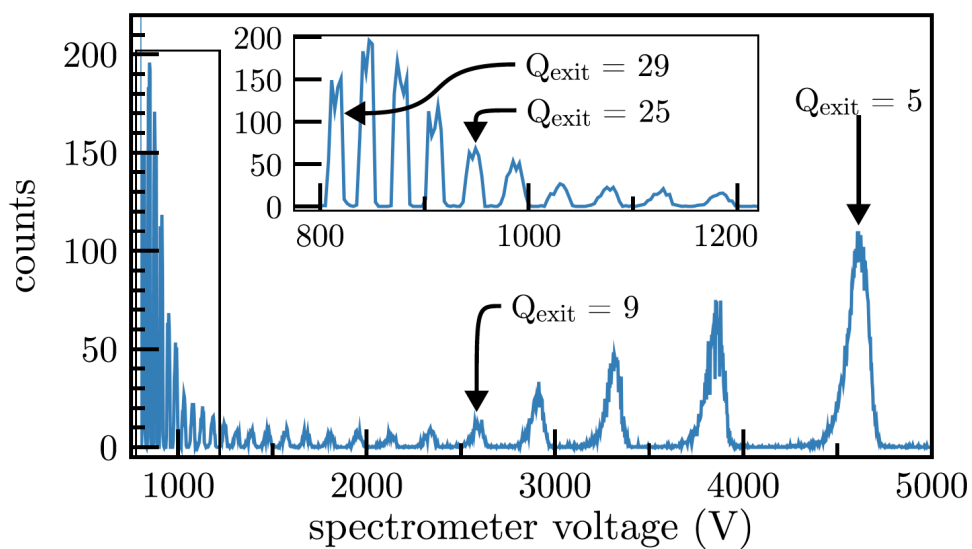


Figure 1.1: Spectrum of a  $\text{Xe}^{30+}$  beam with 1050 eV/amu of kinetic energy transmitted through a 1nm thick CNM sample. In contrast to fig. 1.6 two distinct distributions can be observed. The high exit charge state distribution is magnified in the inset. Taken from [1]

## C. Aim of this thesis

The objective of this thesis was to build the new setup NIELS, which enables to reproduce existing results and to extend the latter with regards to new material like boron nitride (insulator) or molybdenum disulfide (semiconductor), higher energies up to 360 keV and higher angular resolution of about  $0.02^\circ$ . Furthermore, NIELS will be used to irradiate different 2D samples to modify the lattice of 2D materials or form nanostructures.

To quantify energy losses NIELS uses time of flight measurements (TOF). Here the emitted electrons from the interaction process embody a possible option for the start signal production, while a position sensitive imaging multi channel plate (Roentdek Delay line detector) provides a stop signal. Within a short period of time (1hour) between several hundreds to tens of thousands ions per charge state are leaving the source. Thus NIELS enables to reduce the time of measurement crucially compared to previous used electrostatic analyser in Dresden. This property is important for samples, which are degrading due to the ion beam and therefore can only be used for measurements for a short duration.

NIELS is designed to enable coincidence measurements of electronic emission statistics and TOF measurements of 2D materials. In the second chapter I will give an introduction of the principles of electron beam ion source (EBIS) and TOF spectroscopy and discuss the experimental setup NIELS and its specific parameters. First results are presented in chapter 3 followed by a summary and an outlook in chapter 4.



## 2 Experimental setup

In this present chapter an elucidation of the principles of the electron beam ion source (EBIS) and time of flight spectroscopy (TOF-spectroscopy) is given, followed by an overview of the most important components of NIELS with regard to angular resolved TOF-spectroscopy (see figure 2.1) and a short description of them. Furthermore NIELS very own parameters with regard to TOF-spectroscopy and different methods to generate start and stop signals including their benefits and downsides are discussed.

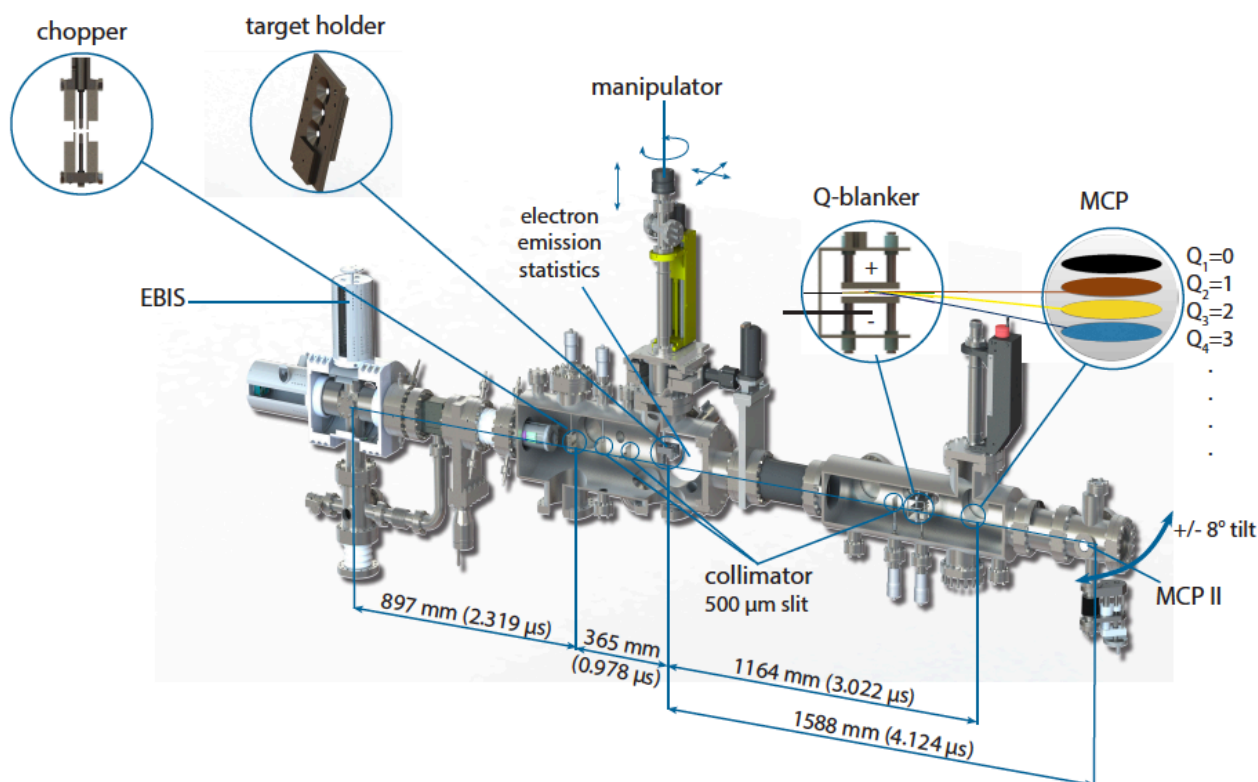


Figure 2.1: Sketch of Niels alongside the whole TOF-spectroscopy beamline, whereby the significant distances and most important components are labeled. Typical flight times are given for 100keV/amu  $Xe^{q+}$  projectiles.

## A. Ion Source

The Dreebit EBIS-A is a room temperature ion source. It is equipped with a Wien filter enabling the selection of a specific charge state from the extracted ion beam. In an EBIS a high-density electron beam collides with atoms and ions. Subsequent ionization results due to the kinetic energy transfer from the electrons of the beam to the electrons of the atom or ion. The source provides highly charged ions of different charge states  $q$  (for example  $Xe^{1+}$  to  $Xe^{46+}$ ) at kinetic energies ranging from  $100 \text{ eV} \cdot q$  to  $12 \text{ keV} \cdot q$ .

### 1) Working principle

A Dreebit EBIS-A is based on a cathode, which generates a strong electron beam that is magnetically compressed to achieve high electron beam densities (see figure 2.2). The electron beam ionizes particles whichever are injected through a small tube into a drift tube ensemble in the middle of the ion source by electron impact ionization. Here they are trapped in the middle drift tube with potential  $U_a$ , which is surrounded by two drift tubes with potential  $U_0$  on the one side and  $U_b$  on the other side. The potentials  $U_0$ ,  $U_a$  and  $U_b$  form a potential trap in axial direction. Radial trapping is realized by the negative space charge of the electron beam.

The EBIS-A can be operated in pulsed mode and leaky mode. When the last drift tube potential is lowered ions with sufficient kinetic energy can leave the trap. This operation mode is called “leaky mode”. Since the particles were solely ionized in the middle drift tube with the potential  $U_a$  they leave the assembly with the kinetic energy

$$E = q \cdot U_b \quad (2.1)$$

whereby  $q$  is the charge state of the ions.

Furthermore the Dreebit EBIS can be operated in “pulsed mode”; here the trap potential changes for a short period of time (20 ns up to 100  $\mu$ s) from  $U_{b1}$  to  $U_{b2}$ , whereby  $U_{b2}$  is smaller than  $U_{b1}$ . As a result, the ions overcome the  $U_{b2}$  potential well although they have not enough energy to get out of the  $U_{b1}$  potential well. For pulse shaping of the transition from  $U_{b1}$  to  $U_{b2}$  an additional electronic has to be used [34-38].

Subsequently the beam is focused and extracted from the ion source by an electrostatic extraction electrode on which a negative potential  $U_{\text{ext}}$  is applied. Because of the repellent force of the  $U_{\text{ext}}$  segment, the electrons are diverted and hit the water-cooled segment wall, which is grounded. After the extraction segment the ions proceed to a Wien-filter through which a certain charge state can be selected.

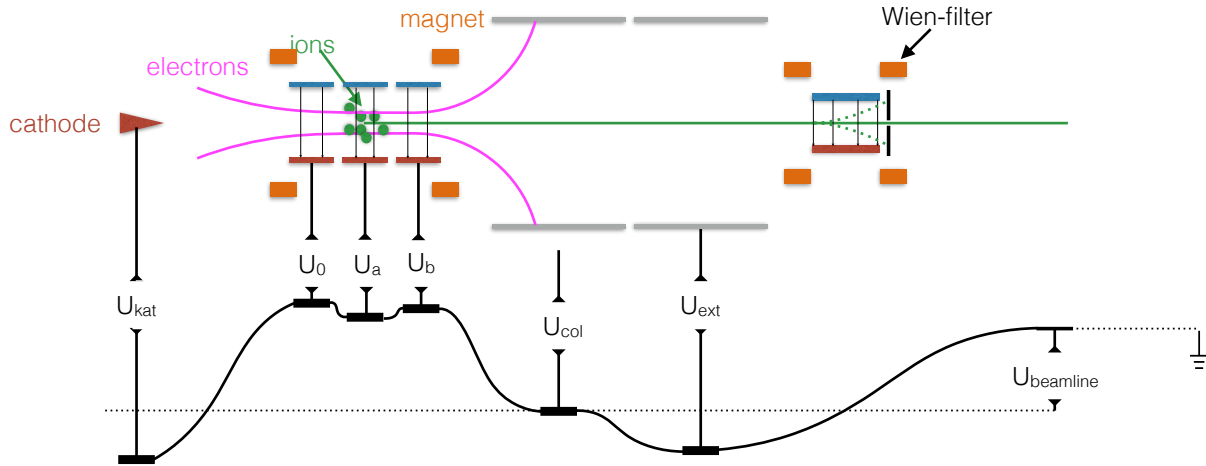


**Figure 2.2:** Simplified sketch of the EBIS-A that depicts the hot cathode for electron production, the magnets and drift tubes, which are necessary for the ion trap. Furthermore one can see the water-cooled electron collector, extraction tube and Wien filter for charge state selection. Underneath the corresponding potentials are shown, whereby the potentials  $U_0$ ,  $U_a$ ,  $U_b$  form the axial ion trap, while  $U_{\text{beamline}}$  enables to decelerate the ions when leaving the source.

Another important feature of our setup is the option to decelerate the ions and therefore reduce their kinetic energy. This is possible because the source can be biased on the potential  $U_{\text{beamline}}$  while the rest of the experiment is grounded (see figure 2.2). If the source is biased on the negative potential  $U_{\text{beamline}}$  the kinetic energy  $E_{\text{kin}}$  is reduced to:

$$E_{\text{kin}} = q \cdot (U_b - U_{\text{beamline}}) \quad (2.2)$$

At the moment it is not possible to apply a higher deceleration voltage than 1500 V, because the power supply is limited to 500  $\mu\text{A}$  output current and the impure laboratory cooling water is already strongly conductive at small voltages (specific conductivity of approx. 200 $\mu\text{S}/\text{cm}$ ).

## II) Important parameters of the EBIS-A

The finite beam diameter and the small voltage offsets of the source have to be validated in order to get correct results (see below).

### a) Beam diameter

After the ion beam has emerged the source, passed the collimator slits and the samples with diameters of 2.7 mm, the particle beams diameter is approximately 3 mm at the MCP (see yellow area at Xe<sup>8+</sup> in figure 2.15).

### b) Source parameter - (U<sub>0</sub>-U<sub>b</sub>-U<sub>d</sub>deacceleration) validation through TOF with deceleration voltages.

Since we plan to perform high-precision measurements, starting voltages have to be validated, to measure energy losses due to ion-solid-interactions properly. Therefore three different charge states  $q$  (19+, 20+, 21+) of Xenon were accelerated with four different starting voltages  $U$  (8799.69 V, 8299.69 V, 7799.69 V, 7299.69 V) and then the TOF-results have been compared. To this purpose the measured time was plotted over the starting voltage. Afterwards one receives through the graphical fit (figure 2.3):

$$E_{kin} = q \cdot e \cdot U \quad (2.3)$$

$$\frac{m \cdot v^2}{2} = \frac{m \cdot \left(\frac{s}{t}\right)^2}{2} = q \cdot e \cdot U \quad (2.4)$$

$$t = s \cdot \sqrt{\frac{m}{2 \cdot q \cdot e \cdot U \cdot b}} \quad (2.5)$$

the adjustment factor  $b$  of the adjusted voltages and thus the actual value.

The graphical fit exposed that the power supplies provide a small inconsistent offset of 2-30 V. Consequently before a valid TOF spectrum can be measured another TOF spectrum without target must be recorded to calibrate the actual initial kinetic energy  $E_{kin} = q \cdot e \cdot U$  of the ion.

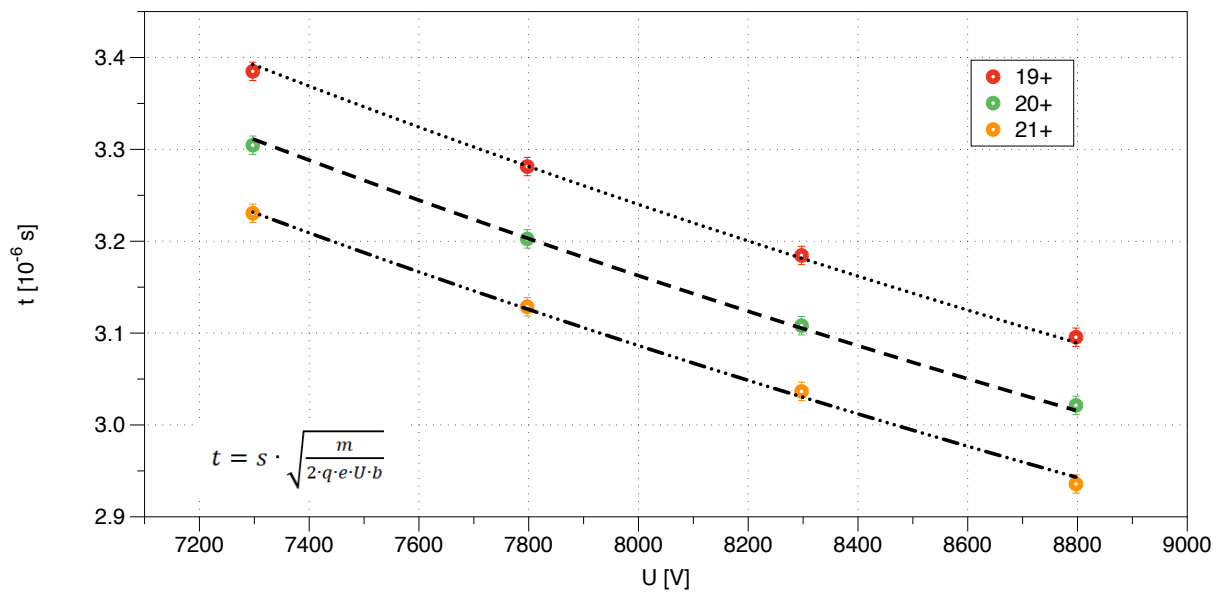


Figure 2.3: Graphical fit of the voltages applied in the source, to evaluate the offset of starting energy.

### c) Charge-state-spectrum

It is important to know which charge states leave the source, therefore it is useful to have a valid charge-state-spectrum available. Hereby the ion current is measured as a function of the Wien-filter voltage.

It is crucial to keep in mind, that even after long time of pumping the base pressure inside the source is about  $10^{-10}$  mbar and consequently also residual gas particles will get ionized.

Figure 2.4 shows such a spectrum, which was recorded on the target holder. Hereby the ion current is measured with regard to the adjusted Wien filter voltage, whereby  $\text{Xe}^{41+}$  is the highest visible charge state. The highest peaks  $\text{Xe}^{8+}$  and  $\text{Xe}^{9+}$  of this particular spectrum are superimposed with the residual gas peaks  $\text{O}^{1+}$  and  $\text{N}^{1+}$ , hence at the moment this spectrum was recorded these Xenon peaks were not usable for a Xenon transmission spectrum.

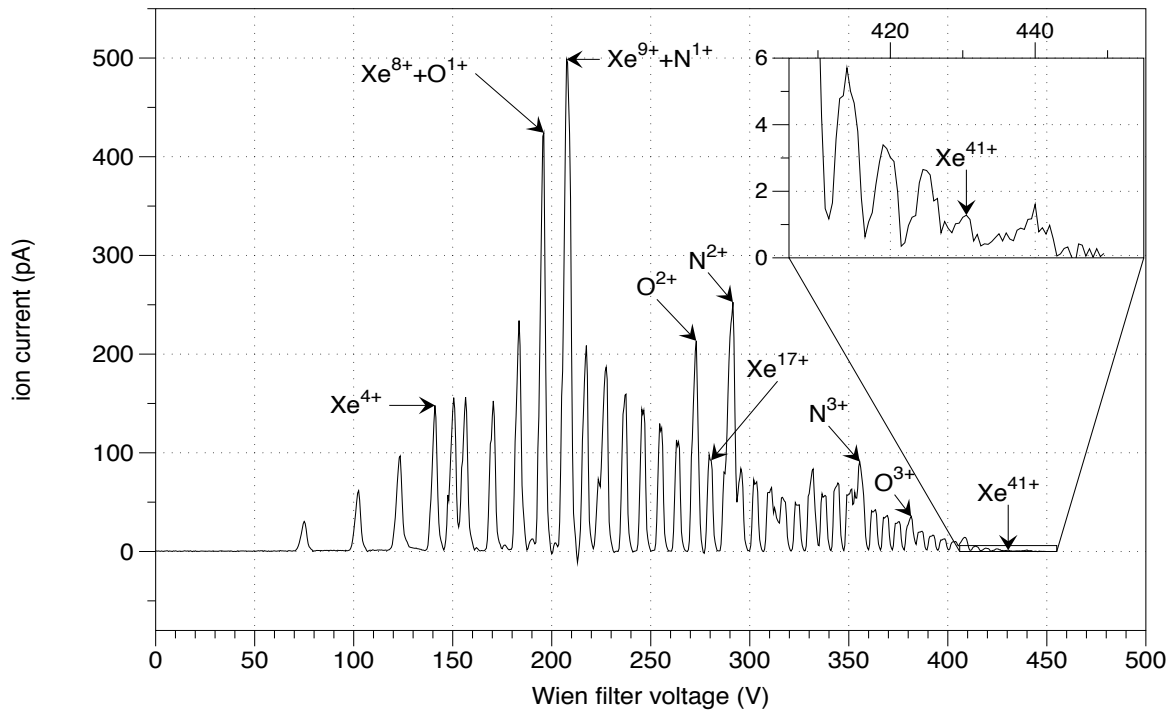


Figure 2.4: charge-state-spectrum of NIELS

## B. Time of Flight (TOF)

Time of Flight-spectrometry (TOF-spectrometry) describes a long known and commonly used method for particle identification. Initially TOF -spectrometry was used to distinguish between neutrons and  $\gamma$ -radiation, which emerges while neutrons are interacting with matter [41]. As a result of the large interest in investigations of nuclear reactions, in which neutrons are emitted, the development of TOF was intensely promoted.

The most valuable characteristics of this method are the good energy resolution at small energies and the applicability for charged and uncharged particles.

## I) Principle of the TOF –spectroscopy

The principle is simple (see figure 2.5), the time, in which a particle travels along a distance, is measured, which yields to the velocity and finally to the kinetic energy of the particle insofar the mass of the particle is known. Therefore a continuous beam of particles out of the particle source is chopped in particle packages of distinct temporal structure. Furthermore precise chronometry plus proper start and stop signals, at the beginning and the end of the defined section, are inevitable. In chapter 2/B/III different types of spectrometry are distinguished by the production of the particle packages besides creation and recording of start and stop signals.

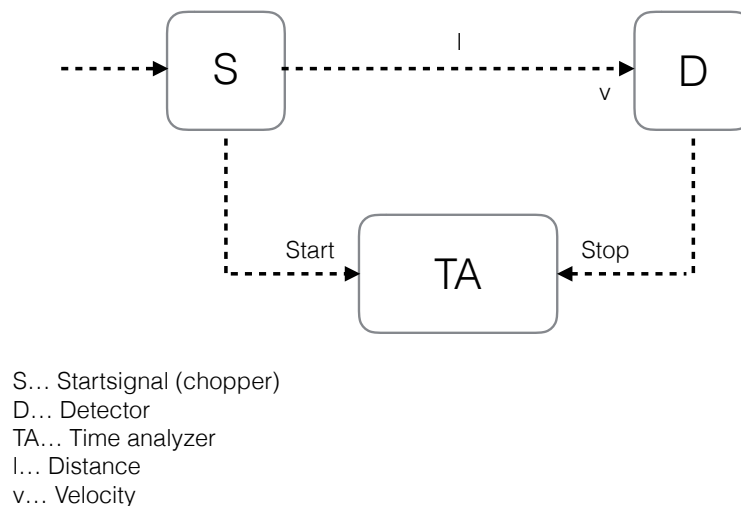


Figure 2.5: schematic setup of time-of-flight-spectroscopy

## II) Resolution of the spectrometer

The time interval, in which the particle travels along the distance, is anti-proportional to the velocity of the particle  $v$  and therefore anti-proportional to the energy  $E$ .

$$E = \frac{m}{2} v^2 = \frac{m}{2} \left( \frac{l_{travel}}{t_{travel}} \right)^2. \quad (2.6)$$

The relative energy resolution of the spectrometer is:

$$\frac{\delta E}{E} = 2 \cdot \frac{\delta v}{v} = 2 \cdot \frac{t_{travel}}{\delta \tau} = 2 \cdot v \frac{l_{travel}}{\delta \tau} \quad (2.7)$$

Thereby  $\delta\tau$  stands for the uncertainty of the measured time-of-flight.  $\delta\tau$  is composed of  $\delta\tau_i$  due to the uncertainty of the initial momentum,  $\delta\tau_f$  due to the width of the distribution of the velocity after sample transmission (energy straggling), the uncertainty of the chronometry  $\delta\tau_c$  and the uncertainty due to geometrical inaccuracy  $\delta\tau_l$  of the observed distances.

$$\delta\tau = \sqrt{(\delta\tau_i)^2 + (\delta\tau_f)^2 + (\delta\tau_c)^2 + (\delta\tau_l)^2} \quad (2.8)$$

Since an electrostatic beam chopper (see section III/b) is the start trigger of the measurement and due to the duration of 20 ns while the chopper is not completely closed, although the ions need only 12 ns to pass the chopper  $\delta\tau_i$  equals 8 ns. The time resolution of the Roentdek delay line detector is below 100 ps, which is the main contribution to  $\delta\tau_f$  and  $\delta\tau_c$ . 10 mm inaccuracy would lead to  $\delta\tau_l$  of 19 ns. Equation 2.8 leads therefore to a gap of about 20 ns.

### III) Production of a start signal

There are several different methods to produce a starting signal. Subsequently I want to give an overview of some options, which can be used in the future operation of NIELS:

#### a) Mechanical beam chopper

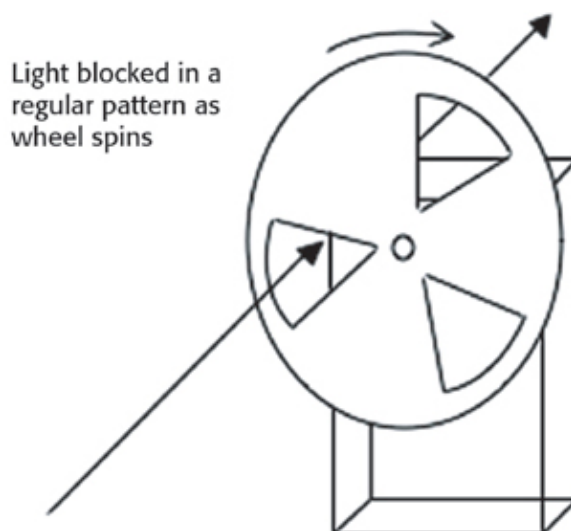


Figure 2.6: Sketch of a mechanical chopper; The slotted disc is driven by an electromotor with a predefined frequency. The measurements of the slots, the rotational velocity and the diameter of the disc are defining the open/close ratio and therefore the length of the particle packages.



The mechanical chopper divides a particle beam in a periodic interval with specific duration and open/close-ratio depending on the rotational velocity, diameter of the chopping vane and slit dimension. Initially this device was used in the 19<sup>th</sup> century to measure the speed of light.

The modern mechanical chopper is basically composed of a mechanical slotted disc and a DC motor, which impels the disc with a certain frequency (see figure 2.6).

The incident beam is directed on a certain radius of the rotating disc of the chopper depending on the requested properties of the beam package. Since the disc moves with a particular frequency the beam is divided in defined intervals. Therefore the layout of the slotted disc and the frequency of rotation define the interval in which the beam is chopped [39].

A high end small size electro motor rotates up to 12 000 rounds per minute, while a maximum diameter of 110 mm for the chopper blades cannot be exceeded due to the inner diameter of 235 mm of our target chamber. This leads to a velocity  $v$  of the edge of the chopper blade of:

$$v = \frac{12\,000 \frac{U}{min}}{60\,s} \cdot 2\pi \cdot 0.11m = 138230 \frac{m}{s} \quad (2.9)$$

Since the beam diameter at the end of the source is about 2 mm and the chopper blade slit has to pass the whole beam the important benchmark is the time it takes to rotate about 2 mm (opening time).

$$\frac{0.002\,m}{138230 \frac{m}{s}} = 14.4 \cdot 10^{-6}\,s \quad (2.10)$$

So if we assume that the slit's width is infinitely small and the chopped blade is 20mm thick the Xe<sup>40+</sup> beam at a kinetic energy of 360 keV needs  $2.7 \cdot 10^{-8}\,s$  to pass the chopper. The sample is therefore exposed for  $14 \cdot 10^{-6}\,s$ , while the beam needs only  $4 \cdot 10^{-6}\,s$  to overcome the 1547mm between chopper and MCP.

The simplicity and the low expenses of the components of this option stands out, unfortunately we cannot use it since the slotted disc would be too big to hedge the needed

kinetic energies the required pulse length and pulse/interim-ratio.

**b) Electrostatic beam chopper**

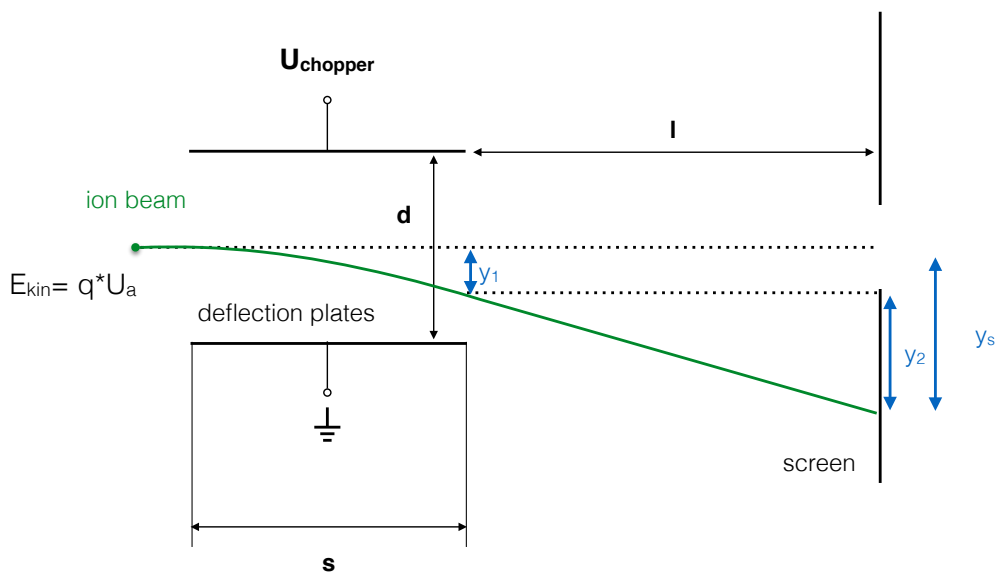
This kind of beam chopping steers the beam away from the slit with the smallest acceptance angle due to a periodic electric field and therefore the detector is receiving particle packages of definite length.

Figure 2.7 exemplifies the deflection process, whereby  $d$  stands for the gap between the two deflector-plates,  $s$  is the length of the deflector-plates,  $U_{chopper}(t)$  describes the time-dependent electrical potential, which is applied onto the deflector-plates. Furthermore a homogeneous monoenergetic ion beam with mass  $m$  and kinetic energy  $q_i \cdot e \cdot U_b$  is considered, which enters the field of the plates assembly. After passing the parallel plates the path  $l$  to the screen is field free [40].

In order to produce sufficient short particle pulses we necessarily had to design and build a new chopper, which when combined with the special electronics is capable to blank voltages of 50 V with a rise/fall time of less than 5 ns [33]. Figure 2.11 depicts the temporal resolution of the chopping regime.

As in the previous discussed method, the chopping process causes immense beam intensity losses, since 99.75% of beam is heading against a wall to attain the desired 10 ns opening time of the pulse and 5  $\mu$ s duration between the pulses.

After the accelerated ions leave the source with the kinetic energy  $E_{kin}$ , they enter the



**Figure 2.7: Principle of the deflection process of the ion beam due to an electrostatic chopper of length  $s$  and plate separation  $d$ ; The process is divided in two sections. In the first section the ions are in between the plates assembly, sense a deflecting force due to the applied voltage  $U_{chopper}$ , which alters the direction of the ion beam and a field free section subsequently the chopper. Therefore the ion beam exits the blunker with a normal distance  $y_1$  from the initial path, but after the travel distance  $l$  the ion beam hits the slit sheet with the much bigger normal distance  $y_s$ .**

deflection plate assembly with the velocity  $v$  determined by:

$$E_{kin} = E_{el} \quad (2.11)$$

$$\frac{m_e}{2} \cdot v^2 = U_b \cdot q_i \cdot e$$

$$v = \sqrt{\frac{2 \cdot U_b \cdot q_i \cdot e}{m_e}} \quad (2.12)$$

whereby  $q_i$  is the charge state of the ions after leaving the ion source and  $U_b$  is the potential the ions are starting from.

Due to the deflection plates of the chopper the particles are solely accelerated in y-direction, so they still perform a uniform motion in x-direction, while in y-direction they now execute a uniform accelerated movement.

$$x = v \cdot t \quad y = \frac{1}{2} \cdot a_y \cdot t^2 \quad (2.13)$$

The deflection voltage  $U_{chopper}(t)$  and the gap between the plates  $d$  lead to the deflection force  $F$  and as a result the acceleration  $a_y$  leads to a diversion  $y$ .

$$F = \frac{U_{chopper}}{d} \cdot q_e \cdot e \rightarrow a_y = \frac{F}{m_e} = \frac{U_{chopper} \cdot q_e \cdot e}{d \cdot m_e} \quad (2.14)$$

$$y = \frac{1}{2} \cdot \frac{U_{chopper} \cdot q_e \cdot e}{d \cdot m_e} \cdot t^2 \quad (2.15)$$

(Note:  $q_e$  is the charge state which is passing the plate assembly and does not necessarily be equal to  $q_i$  (transmission experiment)). After the time  $t_1$ , which the ions need to pass the plates assembly, they are diverted by the distance  $y_1$ , whereby  $q_e$  is the charge state the ions have when they enter the plate assembly

$$t_1 = \frac{s}{v} \rightarrow y_1 = \frac{1}{2} \cdot \frac{U_{chopper} \cdot q_e \cdot e}{d \cdot m_e} \cdot \left(\frac{s}{v}\right)^2 \quad (2.16)$$

When the ions have left the deflection plates the velocity in x-direction  $v_x$  is still the same while the velocity in y-direction  $v_y$  is now finite.

$$v_x = v \quad v_y = a \cdot t_1 = \frac{U_{chopper} \cdot q_e \cdot e}{d \cdot m_e} \cdot \frac{s}{v} \quad (2.17)$$

Between the parallel plates assembly and the slit sheet no external force is exerted on the ions. During the time  $t_2$  the particles travel from the chopper to the screen throughout  $t_2$  ions are further diverted by  $y_2$ .

$$t_2 = \frac{l}{v} \rightarrow y_2 = v_y \cdot t_2 = \frac{U_{chopper} \cdot q_e \cdot e}{d \cdot m_e} \cdot \frac{s}{v} \cdot \frac{l}{v} \quad (2.18)$$

Adding up to a total diversion  $y_s$  from the initial path the ions would have taken, if they wouldn't have passed the plates assembly

$$y_{screen} = y_1 + y_2 \quad (2.19)$$

$$y_{screen} = \frac{1}{2} \cdot \frac{U_{chopper} \cdot q_e \cdot e}{d \cdot m_e} \cdot \left(\frac{s}{v_0}\right)^2 + \frac{U_{chopper} \cdot q_e \cdot e}{d \cdot m_e} \cdot \frac{s}{v} \cdot \frac{l}{v} \quad (2.20)$$

$$y_{screen} = \frac{U_{chopper} \cdot q_e \cdot e}{d \cdot m_e} \cdot \frac{s}{v^2} \cdot \left(\frac{s}{2} + l\right) \quad (2.21)$$

$y_s$  can also be written in means of the acceleration voltage  $U_a$ , applying equation 2.12.

$$y_{screen} = \frac{1}{2} \cdot \frac{U_{chopper} \cdot q_i}{U_b \cdot q_e} \cdot \frac{s}{d} \cdot \left(\frac{s}{2} + l\right) \quad (2.22)$$

With the aid of figure 2.8 I want to discuss three different situations for the ion beam in the specific electric square waved AC field. While the particles of the blue beam enter the chopper at  $t_1$  they undergo within the entire flight through the plate assembly a downward directed force. These particles leave the deflector before the electric field changes.

After the particles of the red beam entered the parallel plates at  $t_2$  the electric field has changed from finite to zero. The temporal downward force on the particles is still strong enough to prevent the particles from passing the slit.

The "green beam"-particles enter the chopper at  $t_3$  while the chopper is almost open and therefore just get slightly dislocated from the path they would have taken if there would not been any force at all.

In summary the green beam particles pass the slit, while the red and blue beam

particles' deflections are too big and therefore will not pass the slit.

Because of the finite beam width particles can pass the slit even when they enter the parallel plates shortly before or after the particles of the green beam. Therefore the finite beam cross section, the chopper and slit geometry and the time-shaping of the chopper voltage lead to a broadening of the time-of-flight, which must be taken into account.

At the moment we are using this method because it is convenient to handle and the prospective significant property of this experiment, coincidence measurements due to electron statistics as start signal, is not mounted yet. The finite beam cross section, the chopper and slit geometry and the time-shaping of the chopper voltage lead to a broadening of the time-of-flight, which must be taken into account.

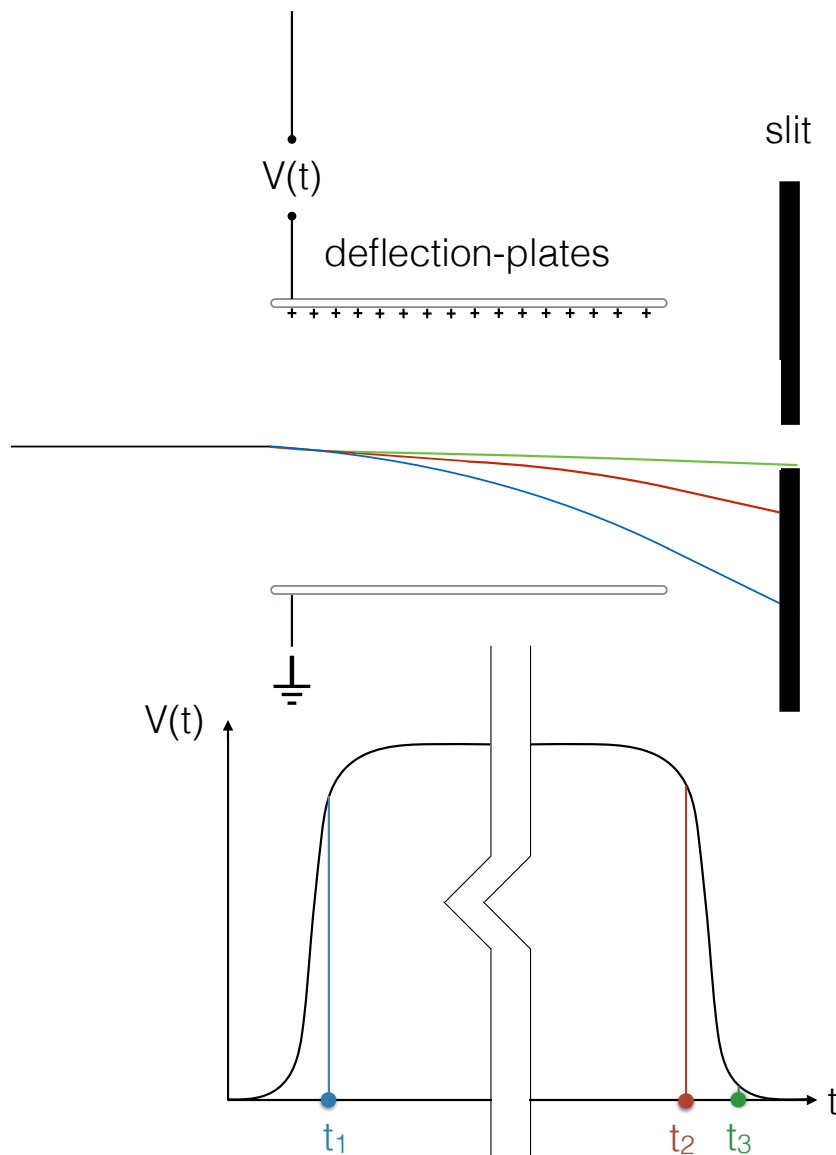


**Figure 2.8: Deflection processes of the ion beam in the electrical AC field; Depending on the moment ( $t_1, t_2, t_3$ ) the ion beam enters the plates assembly the latter experience different deflection force regimes.**

### *c) Pulsing the particle source*

The EBIS can either be used in the “leaky”-mode or pulsed mode. As discussed before in the pulsed mode the potential  $U_b$  is alternating between two predefined values  $U_{b1}$  (20 V higher than  $U_a$ ) and  $U_{b2}$  (20 V lower than  $U_a$ ). Since  $U_{b1}$  is larger than  $U_a$  it seals the source for a certain period of time, whereas  $U_{b2}$  is smaller than  $U_a$  and thus opens the source (for better understanding see figure 2.2). The ions, which are produced while the source is closed, are extracted when  $U_{b2}$  is active along the beamline within a few 10  $\mu$ s. The achievable charge state in the pulsed mode is strongly depending on the time of containment, so the optimal time of containment must be chosen in regard to the intended charge state. However the highest accessible charge state is not defined simply through time of containment alone, but the electron beam density and electron energy as well. The intensity of a specific charge state is thus increasing exponentially with time starting from 0 and with a maximum at infinite time depending on electron beam density and electron energy.

Therefore it is possible to breed the same charge state both in “leaky”- and pulsed mode. Solely the yield of generated ions can be affected by the chosen mode [9]. To get a sufficient intensity of highly charged ions with the Dreebit EBIS-A, containment times between 50 ms and 2000 ms are common. Therefore we cannot use the pulsing mode of the particle source to generate a start signal, because it is not possible to produce the requested open/close properties of 10 ns opening time and 5  $\mu$ s containment time solely with the particle source.

### *d) Using the electron emission statistics as start signal*

We are pursuing the idea to use the electron emission statistics as start signal for the time of flight detection in the future. When ions impinge on a solid surface among other phenomena, potential and inelastic kinetic energy losses occur. The resulting interaction processes of ions and the solid surface strongly depend on the properties of the target material as, for example, the electronic structure, transport processes, the work function and the surface topography, as well as on the potential and kinetic energy of the impinging ion. One major effect phenomenon is the electron emission, which can be subdivided into two regimes, the kinetic electron emission and the potential electron emission. While the kinetic electron emission results from the momentum and energy

transfer of the projectile to an electron of the solid target, the potential energy emission arises due to the initially stored energy in the ion converted into electronic excitation of the target, causing emission of slow electrons. The potential energy emission launches already before the ion first contacts the sample, because the electrons perform fast electron transitions from the surface into empty projectile states (hollow atom) [10,11] above the Coulomb barrier. The spare electrons created in the interaction region are extracted by a weak positive electric field (150 V for an impact angle  $\vartheta$  with respect to the impinging ion beam), applied to a highly transparent grid made of thin wires. The latter is affixed, so that the gap between target and grid is as narrow as possible to achieve high electron collection efficiency. Behind the grid the electrons are attracted by a passivated implanted planar silicon (PIPS) detector biased at high voltage (+30 kV) (see figure 2.9).

Due to the large speed of the electrons caused by the high voltage, the electrons need for the 50 mm to the grid roughly 7 ns, for further 150 mm to the 30 kV biased PIPS detector the electrons need about 1 ns, resulting in 8ns for the electrons from the target to the detector, while it takes the  $\text{Xe}^{20+}$  ions 2.4  $\mu\text{s}$  for the 1182 mm from the target to the nearest MCP leading to a relative timing uncertainty of 0.4 %.

Currently we are not using this option, since the PIPS detector is at high voltage, therefore an optical waveguide made of glassfiber and a specific electronic is necessary to convert it to a suitable start signal for TOF-spectroscopy.

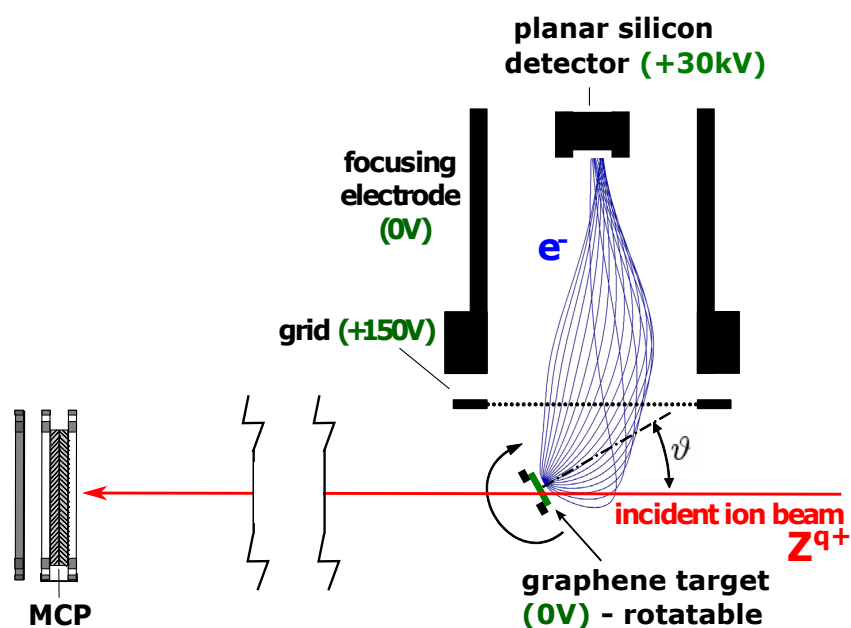


Figure 2.9: The target emits electrons, which form an option for a starting signal for TOF-spectroscopy. The multichannel plate (MCP) is used to register the traversing ions and therefore embody the stop signal, the planar silicon detector with the positively biased grid arranged in front of it, determine the numbers statistics of emitted electrons from the sample (adapted from [42])

#### IV) Important parameters for the TOF-spectroscopy

Every setup has its very own parameters, subsequently you find an overview of the important factors for TOF spectrometry. Furthermore the CAD-Drawings of the chopper, Q-banker, target holder, TOF-chamber and target-chamber are in the appendix.

##### a) *Distance between chopper and target*

For evaluation purposes the distance between chopper and target, the gap of the centers of the two flanges through which we manipulate these two components was determined and resulted in 365 mm.

##### b) *Distance between chopper and MCP*

Here we gathered TOF spectra with different charged states (19+, 20+, 21+) of Xenon and different starting voltages (8799.69 V, 8299.69 V, 7799.69 V, 7299.69 V). The energy and charge states were converted to velocity and plotted over the measured time, which the ion needs to get from the chopper to the first MCP (Roentdek Delay line detector). Afterwards the data was approximated with the fit:

$$v = \frac{a}{t} \quad (2.23)$$

which lead to a distance of  $a = 1547$  mm between chopper and MCP (see figure 2.10).



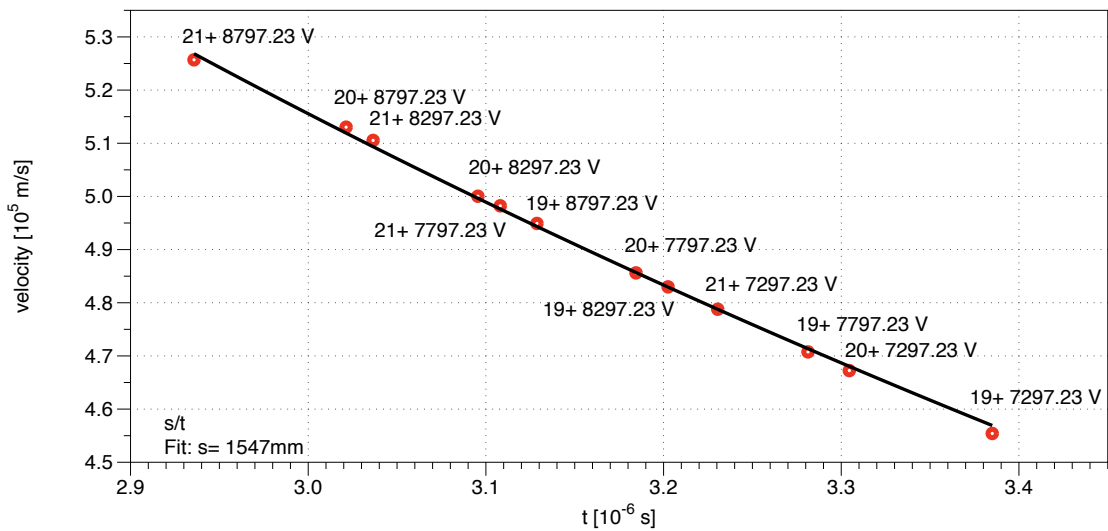


Figure 2.10: Graphical fit of the distance between chopper and MCP (Roentdek Delay line detector)

### c) Chopper voltage

Since the start signal and thus the chopper is essential, it is important to know which voltage is deflecting the particle beam enough, so that no beam gets through the 125 mm distant first 0.5 mm collimator slit and is therefore chopped off (compare with figure 2.1). Empirical analysis has shown that 44.5 V is necessary to chop the ion beam completely off.

### d) Chopper signal passage of time

To get reasonable results it is necessary to optimize the chopper opening time, so that it is open just long enough to let the charged ion pass the chopper and close afterwards again. This is important to receive unslurred TOF-results and therefore as precise as possible energy loss measurements. Figure 2.11 displays the regime of the voltages that are applied on the chopper plates. The green signal represents the actual trigger, a square wave signal caused by a signal generator, which enables to adjust the frequency and the open/closed ratio. This signal is transferred to a waveform generator that converts the signal to a TTL pulse (orange signal). The latter triggers a newly designed fast pulsing electronics [33] that applies the voltages to the plates assembly, whereby the blue signal represents the voltage regime for the upper deflection plate and the red line signifies the voltages applied to the lower plate. To improve the timing-performance, the circuit is equipped with two potentiometers that act as RC circuit alignment. As mentioned before 44.5 V is needed to chop the beam completely off, but

because of “ringing” of the lower plate -35 V was applied on the lower plate and 60 V on the upper plate to prevent a second TOF peak to arise. After each regime the chopper is  $5 \mu\text{s}$  closed to avoid that two consecutive events are overlying each other.

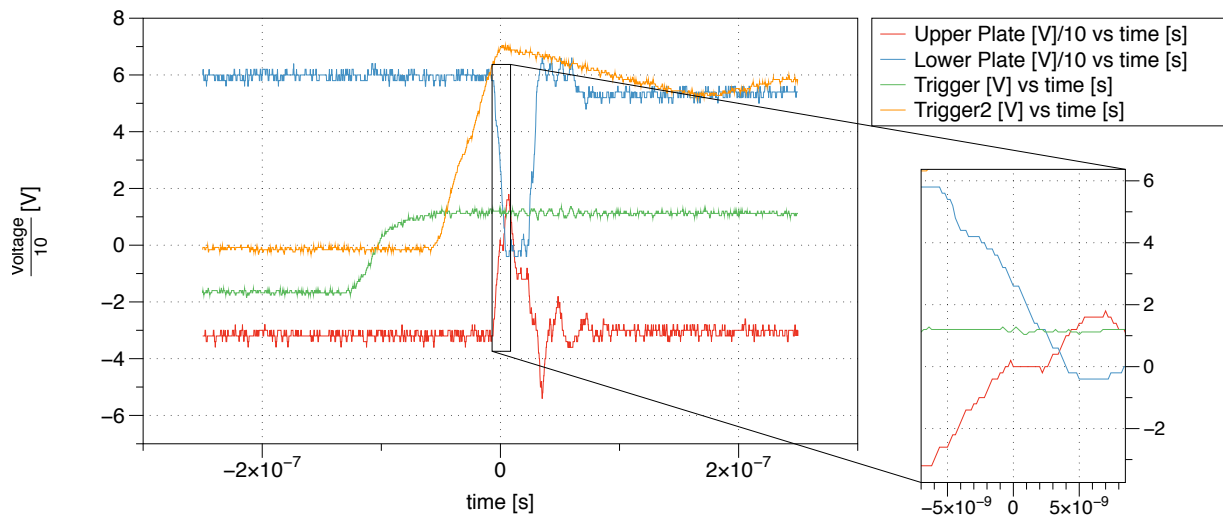


**Figure 2.11: Temporal regime of the applied voltages, whereby the green line represents a TTL pulse, which embodies the actual trigger signal, the orange signal is from the waveform generator, the blue signal depicts the voltage applied to the upper plate and the red line is the descriptive of the lower plate.**

Please note, that the oscilloscope used for the data acquisition shown in fig. 2.11 has a bandwidth of 100MHz. Therefore frequencies higher than 100MHz cannot be accurately reconstructed, i.e. the fast fall/rise time of about 5ns (200MHz) may not be determined correctly. The displayed ringing of the upper plate potential (red curve) may also be an artefact from this lack of bandwidth. An oscilloscope with a reasonably high bandwidth must be used in future, especially to adjust the RC matching. After the RC matching has been accurately performed all cables (in-vacuum and out-of-vacuum), feedthroughs and BNC connectors must not be replaced.

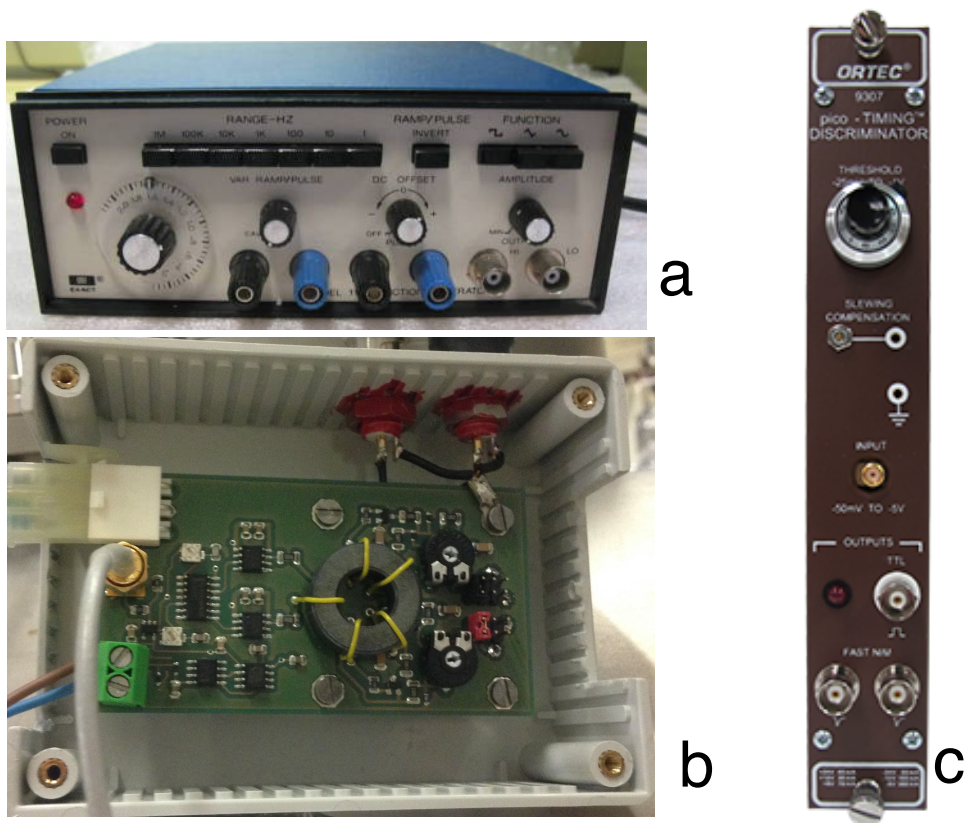


Figure 2.12: Used electrical components for the chopping process; a) Exact function generator model 119 enables to adjust frequency and open/close ratio; b) fast pulsing electronics designed and build by GBS Spezialelektronik for fast voltage pulses on both blanking plates; c) ORTEC pico -TIMING DISCRIMINATOR converts the square wave signal to a TTL trigger signal with 5V height for the fast pulsing electronics.

**e) Timing resolution of the TOF-spectroscopy**

Figure 2.13 shows the TOF measurements of  $\text{Xe}^{21+}$ ,  $\text{Xe}^{20+}$ ,  $\text{Xe}^{19+}$  at 7299,69 V. In the figure one can see that the measurement uncertainty is independent of charge state and velocity. The width of the distribution is always below 10 ns, which leads to a timing accuracy of 0.25 % to 0.3 %, which means that the time of flight of the ions ( $\approx 3\text{-}4 \mu\text{s}$ ) is much larger than the timing resolution.

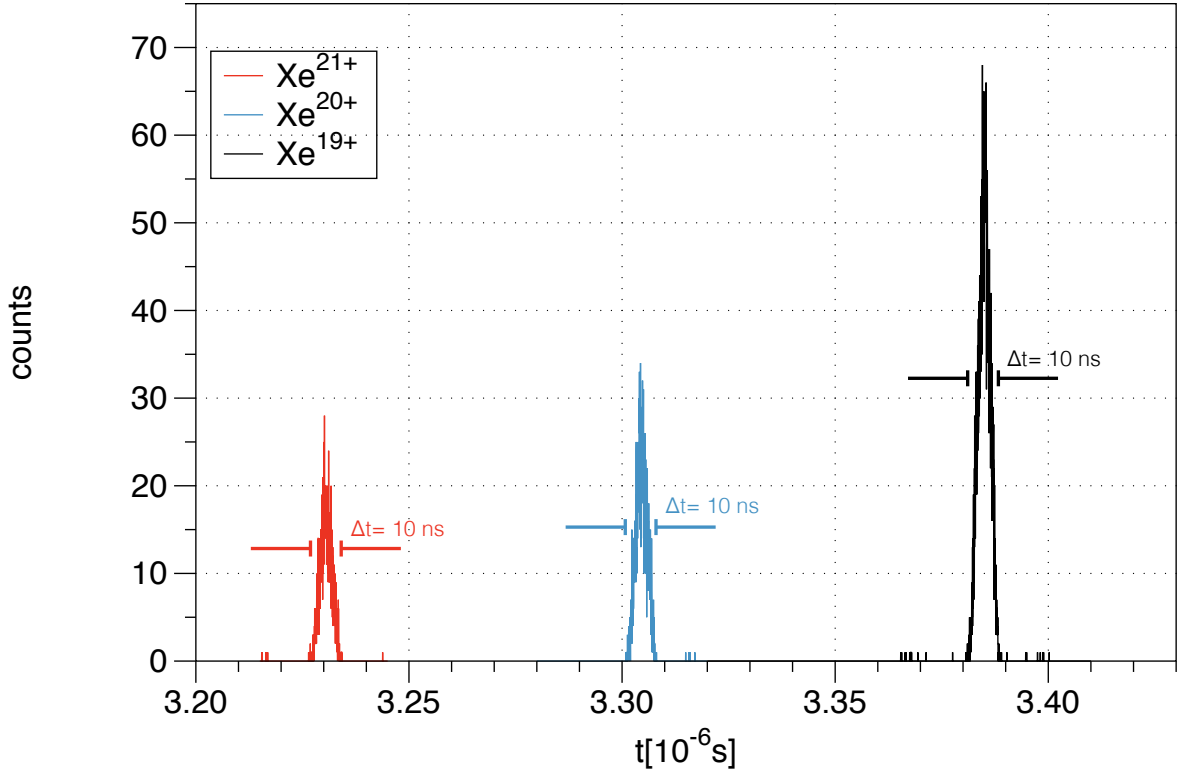


Figure 2.13: TOF measurements of Xe<sup>21+</sup>, Xe<sup>20+</sup>, Xe<sup>19+</sup> at 7299,69 V

However, it is still 0.3 %, which limits the energy resolution  $\partial_E$  to about 1.8 % according to

$$\partial_E = \frac{\Delta E_2}{E_2} \quad (2.24)$$

$$\Delta E_2 = m v_2 \Delta v_2 \quad (2.25)$$

with

$$t = \frac{l_1}{v_1} + \frac{l_2}{v_2} \quad (2.26)$$

$$\Delta v_2 = \frac{1}{t - \frac{l_1}{v_1}} \Delta l_2 + \frac{l_2}{\left(t - \frac{l_1}{v_1}\right)^2} \Delta t + \frac{l_2}{v_1 \left(t - \frac{l_1}{v_1}\right)^2} \Delta l_1 + \frac{l_2}{v_1^2 \cdot \left(t - \frac{l_1}{v_1}\right)^2} \Delta v_1 \quad (2.27)$$

$$\Delta v_2 = 1.41 \cdot 10^4 \frac{m}{s}$$

Whereby table 2.1 shows the used values.

Table 2.1: Values used for the calculation of energy resolution

Symbol	Value	Description
$\partial_E$	1.8 %	Energy resolution
$E_1$		Energy of the particle after leaving the ion source
$E_2$	176 keV	Energy of the particle after passing the target
$m$	129 amu	Mass of the particle
$t$	$\sim 4 \cdot 10^{-6}$ s	Time from chopper to detector
$l_1$	365 mm	Gap between chopper and target
$l_2$	1181 mm	Distance between target and detector
$v_1$	$5.1 \cdot 10^5 \frac{m}{s}$	Velocity of the particle after leaving source
$v_2$	$4.9 \cdot 10^5 \frac{m}{s}$	Velocity of the particle after the target (10% assumed energy loss)
$\Delta E_2$	3.2 keV	Energy uncertainty
$\Delta t$	0.3 % of $t$ $\cong 10ns$	Time uncertainty
$\Delta l_1$	6 mm	Length of the chopper plates
$\Delta l_2$	20 mm	Deviation due to the distance between target and detector due to the movable target
$\Delta v_1$	0.2 % of $v_1$	Deviation of the Initial velocity
$\Delta v_2$	$1.41 \cdot 10^4 \frac{m}{s}$	Deviation of the velocity after passing the target

## C. Collimator

A collimator slit system trims the ion beam, so that optimally a point-like aligned beam is left. Therefore three metal sheets with slits in horizontal direction and one sheet with vertical slits were installed. Each sheet has a slit with 1 mm width and one slit with 0.5 mm width. While the 1 mm slit is mainly used to position the collimator sheet in the ion beam or when the beam intensity is low, in standard operation the 0.5 mm slit is used to achieve better alignment. Two of the horizontal and the vertical collimators were installed between the chopper and the target holder. Since the horizontal sheets are 140 mm apart, the acceptance angle of the 1 mm slits is  $0.409^\circ$  and for the 0.5 mm slits  $0.084^\circ$ . The last horizontal sheet is between sample and Q-blanker to cut the beam in y direction after interactions with the solid surface of the target. This is necessary because otherwise the angular split up due to interaction with the target atoms would interfere with the charge dependent split up due to the static Q blanker potential on the MCP.

## D. Target holder

The special design of the target holder makes it possible to use three different samples and allows to observe ion transmission experiments with an impact angle  $\vartheta$  of as large as  $60^\circ$  with respect to the incident ion beam. At the bottom end of the target holder a Faraday cup is mounted. The mount is movable in all three axial directions, furthermore it is  $360^\circ$  turn-able and can be adjusted remotely, since electric motor are affixed at all axis (compare with figure 2.1). Furthermore an additional small chamber was added separately from the target chamber with a load lock and a separate turbo molecular pump to allow the change of samples in less than an hour and avoiding to vent the target chamber.

## E. MCP

As stop signal for the TOF-spectroscopy we are using an imaging multi channel plate (MCP). After the static field of the Q-blanker separated the distinct charge states we are enabled to see a spatial allocation of different charge states (Roentdek delay line detector) and can use this information to do charge-state-dependent TOF-spectroscopy. Figure 2.14 shows the working principle of such a detector. An impinging particle triggers on the MCP an electron shower, which causes a trigger signal due to the latter hitting the delay line detector DLD. This signal propagate simultaneously in both directions towards the ends of the wire where impedance adjusted circuits pick it up for further processing. The difference of the signal arrival times determine the position of the signal origin both in x and y direction.

Our DLD has a spatial resolution of about 100  $\mu\text{m}$  and a timing resolution of 0.2 ns, the dead time of the Roentdek delay line detector is 10-15 ns and it has a rate capability of 1 MHz.

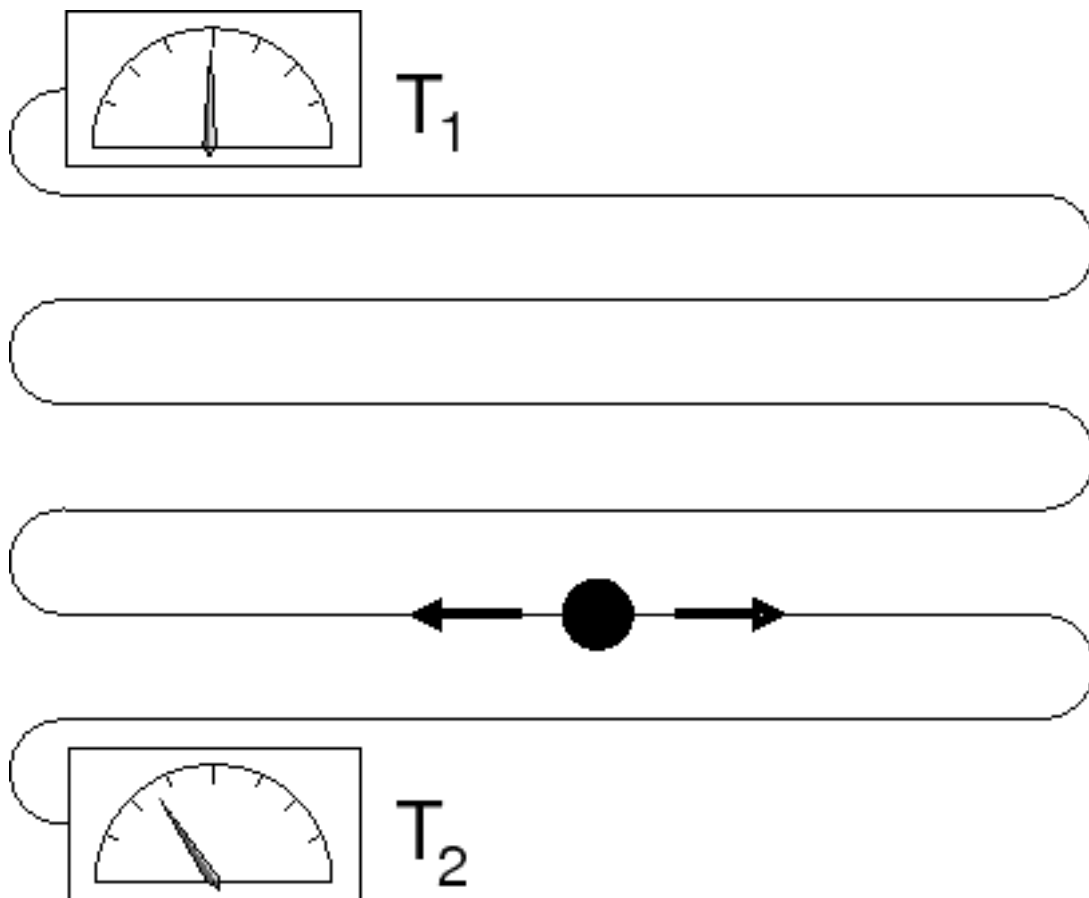


Figure 2.14: Principle of a delay line detector (DLD); The impinging ions trigger an electron cascade in the multi channel plate (MCP), which triggers two signal in the DLD. These signals propagate simultaneously in both directions. Due to the temporal difference of the signals one can determine where the ion initially hit the MCP.

For high-resolution energy loss measurements a second MCP has been installed 417 mm behind the first one. With this increased flight path ( $l_{\text{new}}=1964\text{mm}$ ) the energy resolution  $\partial_E$  changes from 1.8% (DLD) to 1.6% (second MCP). This MCP is used to analyse only one particular charge state at a time, because it has no delay line anode and therefore cannot distinguish between two spatial separated events.

## F. Q-blanker

Since we are working with a position sensitive imaging multi channel plate (Roentdek Delay line detector, see next section) to produce a stop signal, we are able to observe simultaneously different charge states after the ion beam has undergone charge exchange due to interaction processes with the solid surface of a target. This allows us to perform charge-state-dependent TOF measurements. Therefore we installed a parallel plate deflector (called Q-Blanker) in front of the MCP. By setting the plates on a static DC voltage we can separate charge states.

### I) Relation between Q-Blanker deflection voltage and deviation on the MCP

To obtain charge-state-dependent TOF-spectroscopy it is inevitable to know where every single charge state is going to hit the imaging MCP. Consequently it is important to find a relation that determines the position on the MCP. For this relation the distance between Q-Blanker and MCP and the dimensions of the Q-Blanker are of great interest (for derivation see chapter 2/B/III/b):

$$y = \frac{1}{2} \cdot \frac{U_e}{U_b} \cdot \frac{q_e}{q_i} \cdot \frac{s}{d} \cdot \left( \frac{s}{2} + l \right) \quad (2.28)$$



**Table 2.2: Description of used variables**

$y$	Position on the MCP
$U_e$	Voltage between the Q-Blanker plates
$U_b$	Starting voltage in the EBIS
$q_e$	Charge state at the Q-Blanker
$q_i$	Initial charge state
$s$	Length of the Q-Blanker plates
$d$	Distance between Q-Blanker plates
$l$	Distance between Q-Blanker and MCP

Current parameters:

**Table 2.3: current parameters of the Q-blanker**

$s$	39.6mm
$d$	4.6 mm
$l$	117 mm

At the moment we are unable to use the whole height of the MCP, because if more than 230 V are applied onto the Q-blanker plates the ion beam hits the latter. This problem is based on the current narrow dimensions of the Q-blanker, therefore we plan to alter these to fit our needs (for further information see chapter 5, results and discussion).

For validation of the expression and the current parameters, figure 2.15 shows the calculated and the measured positions of the charge states  $Xe^{q+}$  ( $q=1-8$ ) and the neutral Xenon atom, all leaving the source with the same energy as  $Xe^{8+}$  (71 keV).

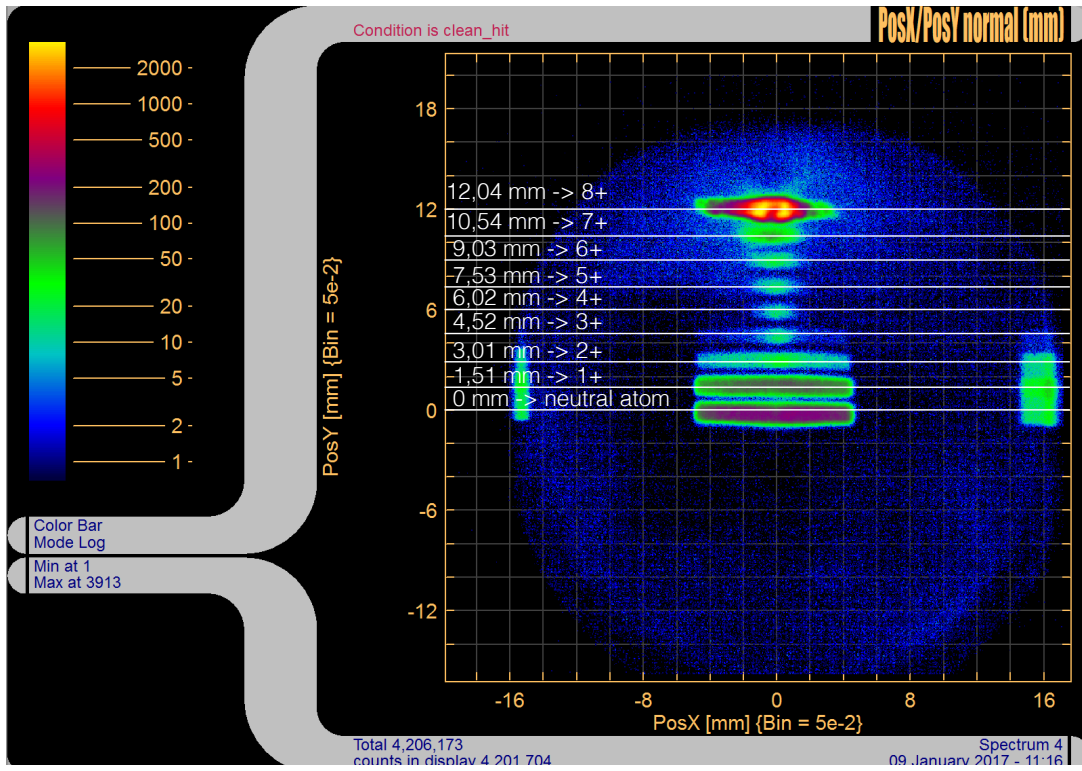


Figure 2.15: Screenshot of a  $\text{Xe}^{8+}$ -CNM-interaction spectrum recorded with CoboldPC2011 Software in comparison to calculated positions for exit charge states shown as white lines.

## 3 Results and discussion

The main purpose of this present work was to design, build and test NIELS. This chapter should give the reader a general overview of the expected output of TOF-spectroscopy and charge state separation received at the MCP (Roentdek Delay line detector). Furthermore I want to validate the stated assumptions from the previous chapters.

### A. TOF-spectroscopy

This section is dedicated to show that we can measure energy loss due to the transmission of an ion through a solid target. For receiving suitable TOF results from the desired sample a proper controlled chopping routine with sufficient short opening times is necessary. Therefore, a major focus in the present work was put on development of a proper chopper, based upon the latter a chopping routine, and on comparing the received results with the ones obtained by computation. For further details please see chapter 2 B.

Figures 3.1 and 3.2 show TOF-spectra with ideal chopper settings (see figure 2.10). While figure 3.1 depicts a spectrum of the ion beam without any interaction with a sample, figure 3.2 illustrates the initially  $\text{Xe}^{21+}$ -beam after going through a carbon nano membrane (CNM) sample, capturing 20 electrons and losing some of its kinetic energy. As one can see, it takes the beam about 10 ns longer to reach the MCP, which equals an energy loss of  $1.2 \text{ keV} \pm 0.24 \text{ keV}$ .

The width of the distributions in figure 3.1 to 3.2 represents the 8 ns opening time of the chopper. This minimum opening time on the other hand depends on the time the ion needs to pass the chopper itself. The electrical chopper is deflecting the beam in a finite time and the diameter of the ion beam the TOF-measurement is not a delta function but slightly slurred.

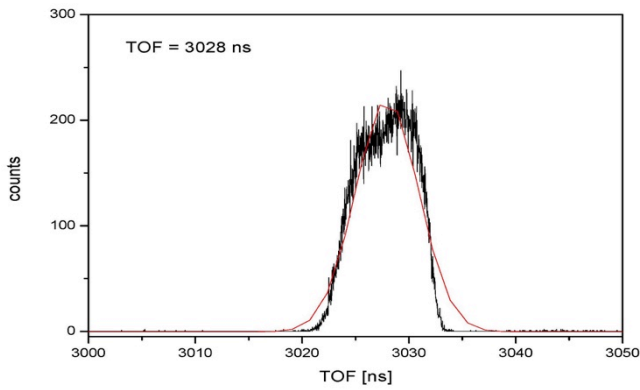


Figure 3.1: TOF-spectrum of  $\text{Xe}^{21+}$  without target

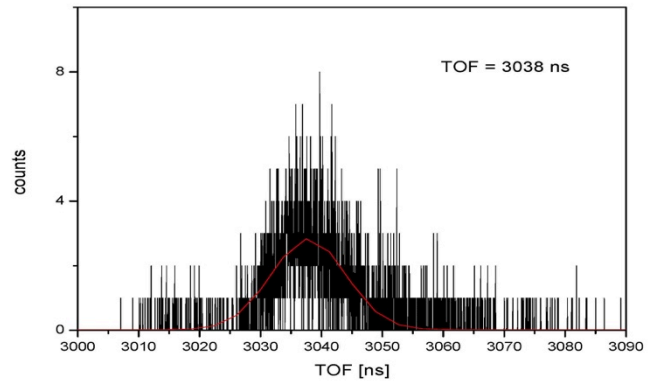


Figure 3.2: TOF-spectrum of  $\text{Xe}^{1+}$  after passing a CNM-target

## B. TOF-spectrum with poor chopper settings

For educational reasons this section shows a poor chopper setting (figure 3.3) and the corresponding TOF-spectrum (figure 3.4). Figure 3.3 exhibits the voltage  $V(t)$  regime of the upper chopper plate, while the other one is grounded. The obvious “ringing” at the beginning of the square wave signal leads to the result that the chopper voltage drops right after it is opened, subsequently it opens again and a few particle can pass the chopper, which therefore produce an additional peak in the TOF-spectrum (see figure 3.4). It is hardly possible to prevent any “ringing” but in cases it occurs the chopper voltage has to be increased up to a value that even “ringing”-valleys do not allow any particle to pass the chopper and the collimator sheets and the impedance of the chopper electronic has to be balanced. Again a proper RC matching performed with a GHz oscilloscope may solve this problem.

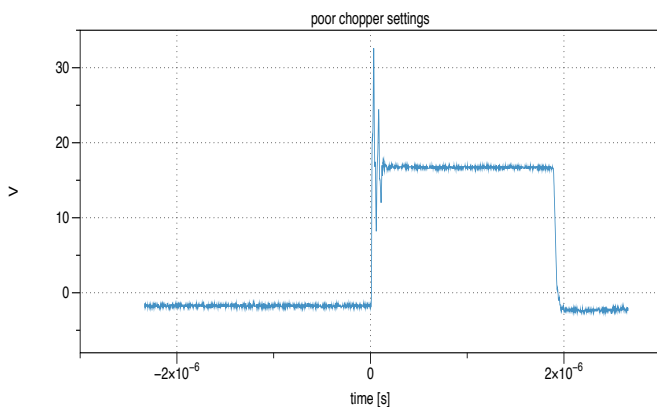


Figure 3.3: Chopper settings which lead to a useless TOF-spectrum

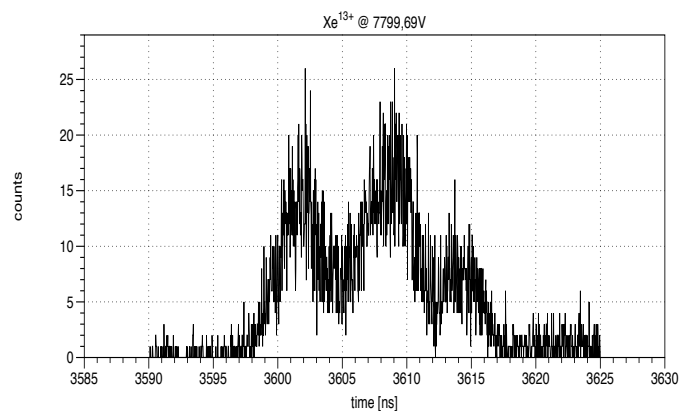


Figure 3.4: TOF-spectrum with poor chopper settings

### C. Charge state spectrum of CNM and graphene target

When the charged ion passes a sample charge exchange processes take place. Since NIELS uses a position sensitive imaging resolving MCP the different charged ions can be visualized by separation of the charge states due to the positive voltage applied to the Q-blanker plates resulting in a charge state spectrum. (for details see chapter 2/A/II/c). Figure 3.5 shows such a spectrum for an initially  $\text{Xe}^{13+}$ -ion after passing a carbon nanomembrane (CNM) sample with all charge states due to charge exchange processes, whereby black represents low intensity and yellow very high intensity. The global maximum corresponds to the original  $\text{Xe}^{13+}$  ion beam. The high exit charge states are well separated from lower local maxima by a comparatively wide low intensity region corresponding to middle charge states below which the intensity rises and the maxima gets spatial broader spread. As one can see in the right plot of figure 3.5 the higher charge states have more intensity (up to  $10^6$  counts) but are not angular distributed (typically  $0.1^\circ$  width in the left plot of figure 3.5). The intensity of the lower charge states  $\text{Xe}^{q+}$  ( $q = 1-4$ ) on the other hand is not as high as the intensity of the higher ones but the charge states show due to interaction with the solid a Gaussian-like angular distribution (in horizontal direction). A model description for the underlying scattering processes is given in [42].

(Note: The maximum scattering angle of Xenon after one hit with carbon is  $5.3^\circ$  and the angular resolution is about  $0.02^\circ$ )

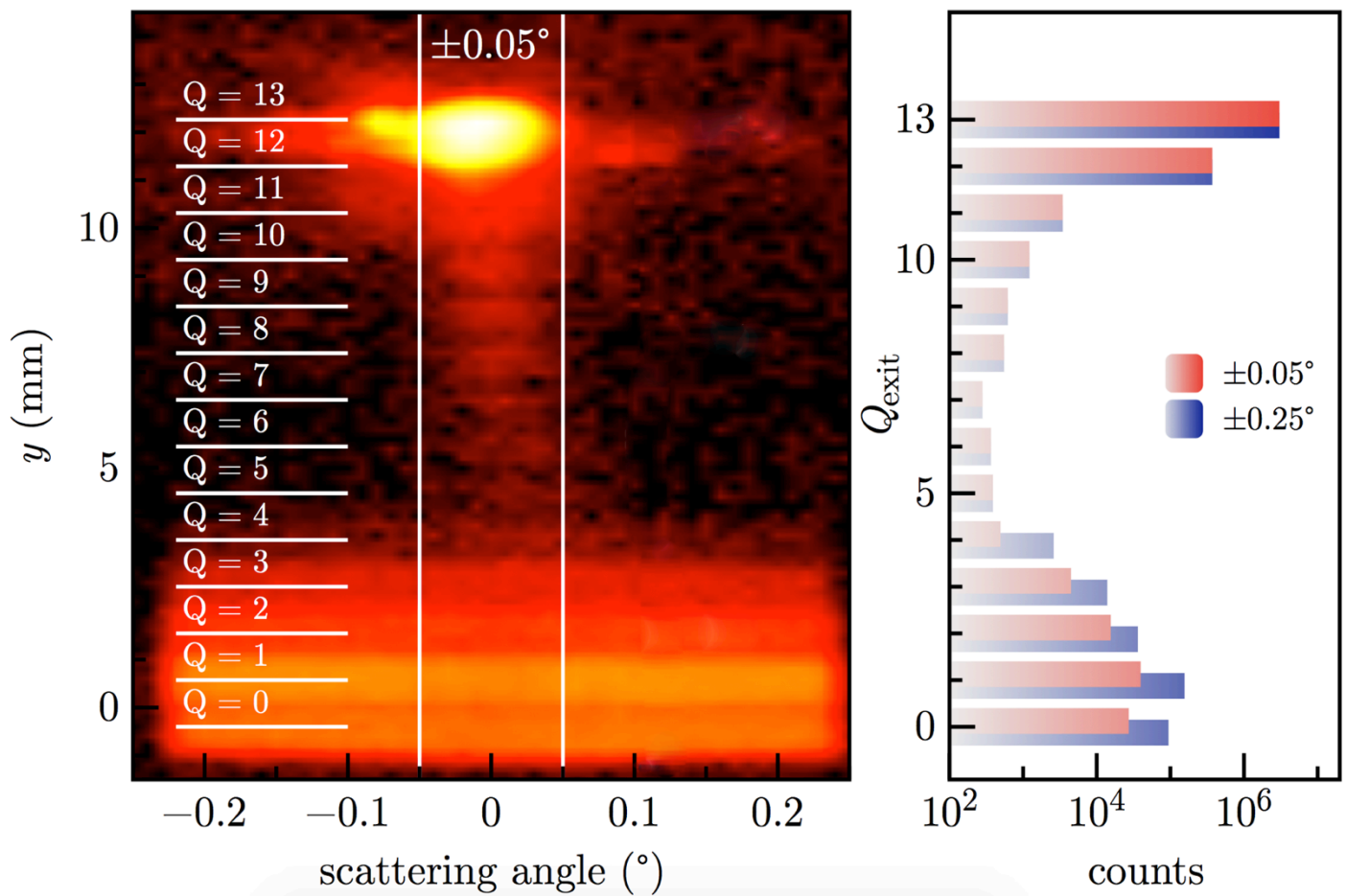


Figure 3.5: Spectrum of the exit charge states after CNM-Xe<sup>13+</sup>-interaction separated by an applied Q-blanker voltage of 180 V; The left plot shows the spatial distribution of the interaction extended with calculated positions of the various states; The right plot depicts the corresponding intensities of the different charge states.

## 4 Conclusion and Outlook

Ion experiments investigating charge exchange processes of ions and electron emission from different materials are already under investigation at the TU Wien for many years [2-7]. With the newly designed and built setup called NIELS we are merging these two information and measure them in coincidence.

As ion source we use a Dreebit EBIS-A as a loan from Helmholtz Zentrum Dresden Rosendorf to generate highly charged ions. For TOF spectroscopy we had to get ion pulses of specific length. For the start signal a custom chopper had to be designed and built, a new target holder design and load lock with a separate turbo molecular pump was mounted. Due to this addition one is able to exchange samples in less than an hour, without the inconvenience of being forced to vent the whole target-chamber for this procedure. For stop signal we are using two MCPs, the one nearer to the target is position sensitive to display the distinct charge states after passing the target. The latter are separated by a static voltage applied to the Q-blanker plates. The MCP further away from target is not position sensitive, but since the ions have to travel longer to trigger the stop signal, it can be used for more precise measurements of energy loss processes of the ion while passing the sample.

For further improvements of the NIELS facility the following steps are being recommended:

### **A. Data evaluation concept**

It is necessary to manage the received data and reasonably operate with them. A program that automates the processing of the spectra would be of great value. First of all the selection of angles, charge states and corresponding TOF values from a list mode file would be very helpful. Additionally the program should be able to calculate the TOF of distinct charge states, depiction of the distribution of the latter and the generation of text files to process the spectra for further application.

## **B. Installation and start of electron emission statistics**

At the moment this thesis is written, the electron emission statistics is not mounted on NIELS. As described in chapter 2/B/III/d operating the electron statistics detector as a start signal generator for TOF will significantly improve the TOF resolution. However, special care must be taken because the statistics detector is operated at high voltage (30kV) and the timing signal must be fed into a time-to-digital converter on ground potential. Using a glass fiber optics for signal transfer is an option provided that the timing information remains preserved.

## **C. Adjustment Q-blanker**

Since we want to utilize the full height of the spatial resolving MCP the Q-blanker must be modified. Therefore the distance between the plates or the length/shape of the plates has to be altered. While the distance can be enhanced by simply shorten the three bolts and spacers on each plate (see appendix for a CAD drawing of the Q-blanker), the length/shape adjustment would be almost as sophisticated as designing and building a new Q-blanker. Therefore the distance is the more convenient way and will take place soon. During the adjustment of the latter, the entrance slit-plate of the Q-blanker will be broadened, so that the width of the MCP is fully covered.

## **D. Replacement of the cooling cycle**

As stated in chapter 4 we are limited with respect to deceleration of the ion beam, as the laboratory cooling water is not pure enough for our experiment. A new cooling system should solve this issue by being closed in itself, so fresh pure water just has to be provided rarely. Depending on the installation site the currently long hose running through the whole lab could be omitted. Thereby another instability factor could be disabled, since at the moment if any of the tabs for the water hose of any of the many experiments in the laboratory collapses the whole water circuit for all experiments is instantaneously turned off.



## **E. Simplification of target exchange**

At the moment it is hard to exchange the samples for one person alone, because one does not see the target well enough. I would recommend to exchange the flange below the target holder to a window, so that the exchange procedure can be monitored and realized by one person only.

## Bibliography

- [1] R. A. Wilhelm et al., *Phys. Rev. Lett.* **112**, 153201 (2014).
- [2] G. Lakits, F. Aumayr, *Rev. Scien. Instrum.* **60**, 3151 (1989).
- [3] F. Aumayr, G. Lakits, *Appl. Surf. Scien.* **47**, 139 (1991).
- [4] H. Kurz, F. Aumayr, *Phys. Rev. A* **48**, 2182(1993).
- [5] C. Lemell, F. Aumayr, *Phys. Rev. Lett.* **81**, 1965 (1998).
- [6] M. Vana, F. Aumayr, *Nucl. Instrum. Methods Phys. Res., Sect. B.* **100**, 284 (1995).
- [7] M. Vana, F. Aumayr, *Europhys. Lett.* **29**, 55 (1995).
- [8] A. K. Geim and K. S. Novoselov. *Nat. Mater.* **6**, 183 (2007).
- [9] J. Burgdörfer et al., *Phys. Rev. A* **44**, 5674 (1991); J. Burgdörfer and F. W. Meyer, *Phys. Rev. A* **47**, R20 (1993).
- [10] F. Aumayr and HP. Winter, *Nucl. Instrum. Methods Phys. Res., Sect. B* **90**, 523 (1994).
- [11] D. H. Schneider and M. A. Briere, *Phys. Scr.* **53**, 228(1996), and references there in.
- [12] J. P. Briand et al., *Phys. Rev. Lett.* **65**, 159 (1990); J.-P. Briand et al., *Phys. Rev. A* **53**, 1 (1996); M. A. Briere et al., *Nucl. Instrum. Methods Phys. Res., Sect. B* **90**, 231(1994).
- [13] T. Schenkel et al., *Phys. Rev. Lett.* **78**, 2481 (1997); *Nucl. Instrum. Meth. Phys. Res., Sect. B* **125**, 153(1997).
- [14] R. Schuch et al., *Phys. Rev. Lett.* **70**, 1073 (1993).
- [15] L. Folkerts and R. Morgenstern, *Europhys. Lett.* **13**, 377(1990).
- [16] S. Winecki et al., *Phys. Rev. A* **53**, 4228 (1996).
- [17] R. Díez Muiño et al., *Phys. Rev. Lett.* **76**, 4636 (1996).
- [18] R. Herrmann et al., *Phys. Rev. A* **50**, 1435 (1994).
- [19] J. Biersack, *Nucl. Instrum. Meth. Phys. Res., Sect. B* **80/81**, 12 (1993).
- [20] M. A. Briere et al., *Phys. Scr.* **53**, 228(1996).
- [21] J. I. Juaristi and A. Arnau, *Nucl. Instrum. Methods Phys. Res., Sect. B* **115**, 173 (1996).
- [22] N. Hatke et al., *Nucl. Instrum. Meth. Phys. Res., Sect. B* **115**, 165 (1996).
- [23] H. Khemliche et al., *Nucl. Instrum. Methods Phys. Res., Sect. B* **125**, 116 (1997).

- [24] E. Gruber et al., *Nat. Comm.* **7**, 13948 (2016).
- [25] R. A. Wilhelm et al. *2D Mater.* **2**, 035009 (2015)
- [26] R. Ritter et al., *Appl. Phys. Lett.* **102**, 063112 (2013).
- [27] R. Zan, et al., *Nano Lett.* **12**, 3936–3940 (2012).
- [28] J. Yu, et al., *Nano Lett.* **12**, 1603–1608 (2012).
- [29] A. D. Liao et al., *Rev. Lett.* **106**, 256801 (2011).
- [30] N. Bohr, *Medd. Dan. Vid. Selsk* **18**, 1 (1948).
- [31] T. Schenkel et al., *Phys. Rev. Lett.* **79**, 2030 (1997).
- [32] A. Ojanperä, et al., *Phys. Rev. B* **89**, 035120 (2014).
- [33] N. Klingner, R. Heller. *Ultramicroscopy* **162**, 91-97 (2016).
- [34] Dresden EBIS-A - DREEBIT | Ion Beam Technology. [online] Dreebit-ibt.com. Available at: <http://www.dreebit-ibt.com/product/dresden-ebis-a.html> [Accessed 11 Jan. 2017].
- [35] G. Zschornack, et al., *Nucl. Instrum. Methods Phys. Res., Sect. B* Vol. 235, Issue 1-4, p. 514-518. (2005)
- [36] U. Kentsch, G. Zschornack, *Rev. of Scien. Instrum.* **73**, 660 (2002).
- [37] LV. Ovsyannikov, G. Zschornack, *Rev. of Scien. Instrum.* **70**, 2646 (1999).
- [38] M. Schmidt, et al., *Rev. of Scien. Instrum.* **80**, 063 301 (2009).
- [39] AZoOptics.com, [online] Available at: <http://www.azooptics.com/Article.aspx?ArticleID=543> [Accessed 20 Nov. 2016].
- [40] J. Bakker, *J. Phys E: Scien. Instr.* **6**, 785, (1973).
- [41] W. Stephens, *Phys. Rev. Lett.* **69**, 691 (1946).
- [42] R. A. Wilhelm, Wechselwirkung langsamer hochgeladener Ionen mit Ionenkristalloberflächen und ultradünnen Kohlenstoffmembranen, phd thesis, Technische Universität Dresden (2014).
- [43] J. Schwestka, Coincidence Measurements of Ion-Induced Electron Emission from Graphene, master thesis, Technische Universität Wien (2016).



# Danksagung

An dieser Stelle möchte ich mich bei all denjenigen bedanken, die mich während der Anfertigung dieser Masterarbeit unterstützt und motiviert haben.

Zuerst gebührt mein Dank Dr. Richard Wilhelm und Prof. Dr. Friedrich Aumayr, die meine Diplomarbeit betreut und begutachtet haben. Vor allem Richard möchte ich für die hilfreichen Anregungen und die konstruktive Kritik bei der Erstellung dieser Arbeit herzlich danken.

Ebenfalls möchte ich mich bei Janine Schwestka bedanken, die mir mit viel Geduld und Hilfsbereitschaft zur Seite stand. Bedanken möchte ich mich für die zahlreichen interessanten Debatten und Ideen, die maßgeblich dazu beigetragen haben, dass diese Masterarbeit in dieser Form vorliegt und ohne die diese Arbeit nicht hätte entstehen können.

Ein besonderer Dank gilt auch Lukas Leonhartsberger, der durch seinen Mut anzupacken diese Projekt stets weitergebracht hat.

Meiner Freundin Kim Grömminger danke ich besonders für den starken emotionalen Rückhalt über die Dauer meines gesamten Studiums.

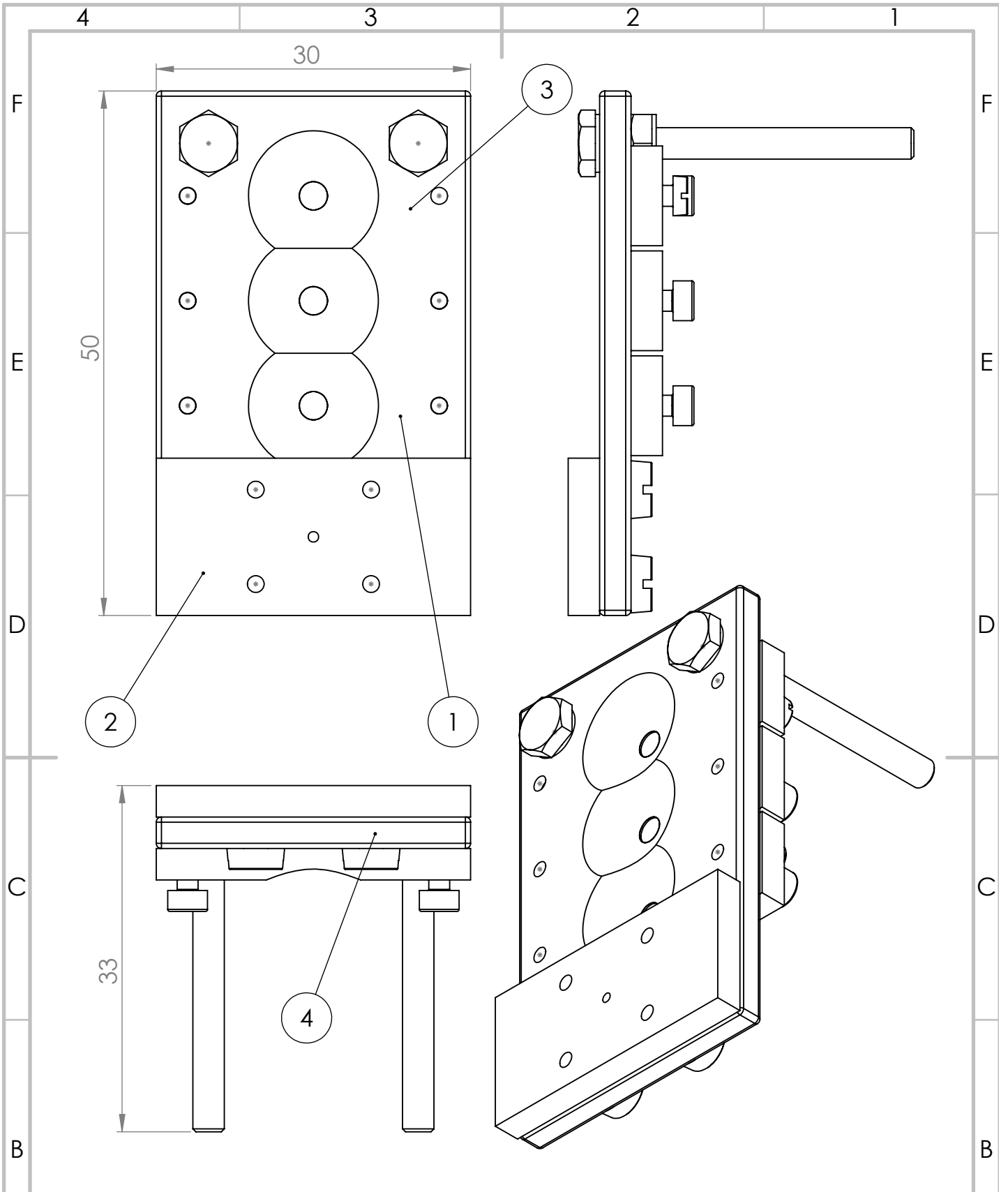
Abschließend möchte ich mich bei meiner Familie bedanken, die mir mein Studium durch ihre Unterstützung ermöglicht hat und stets ein offenes Ohr für meine Sorgen haben.



# Appendix







WENN NICHT ANDERS DEFINIERT:  
 BEMASSUNGEN SIND IN MILLIMETER  
 OBERFLÄCHENBESCHAFFENHEIT:  
 TOLERANZEN:  
 LINEAR:  
 WINKEL:

OBERFLÄCHENGÜTE:

ENTGRATEN  
 UND SCHARFE  
 KANTEN  
 BRECHEN

ZEICHNUNG NICHT SKALIEREN

ÄNDERUNG

	NAME	SIGNATUR	DATUM		
GEZEICHNET					
GEPRÜFT					
GENEHMIGT					
PRODUKTION					
QUALITÄT					

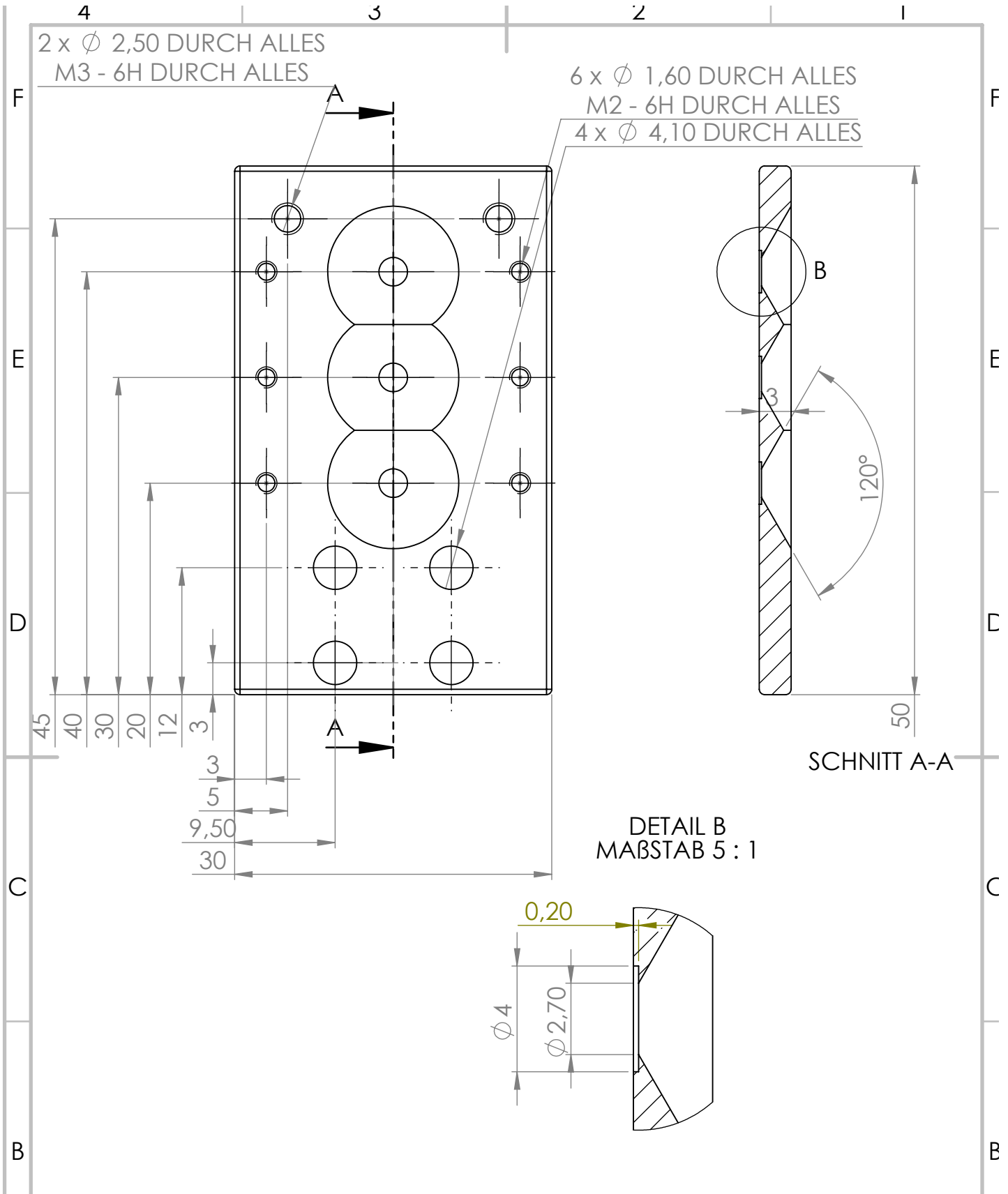
BENENNUNG:

WERKSTOFF:

ZEICHNUNGSNR. Targethalter

A4





WENN NICHT ANDERS DEFINIERT:  
BEMASSUNGEN SIND IN MILLIMETER  
OBERFLÄCHENBESCHAFFENHEIT:  
TOLERANZEN:  
LINEAR:  
WINKEL:

OBERFLÄCHENGÜTE:

ENTGRATEN  
UND SCHARFE  
KANTEN  
BRECHEN

ZEICHNUNG NICHT SKALIEREN

ÄNDERUNG

	NAME	SIGNATUR	DATUM	
GEZEICHNET				
GEPRÜFT				
GENEHMIGT				
PRODUKTION				
QUALITÄT				

BENENNUNG:

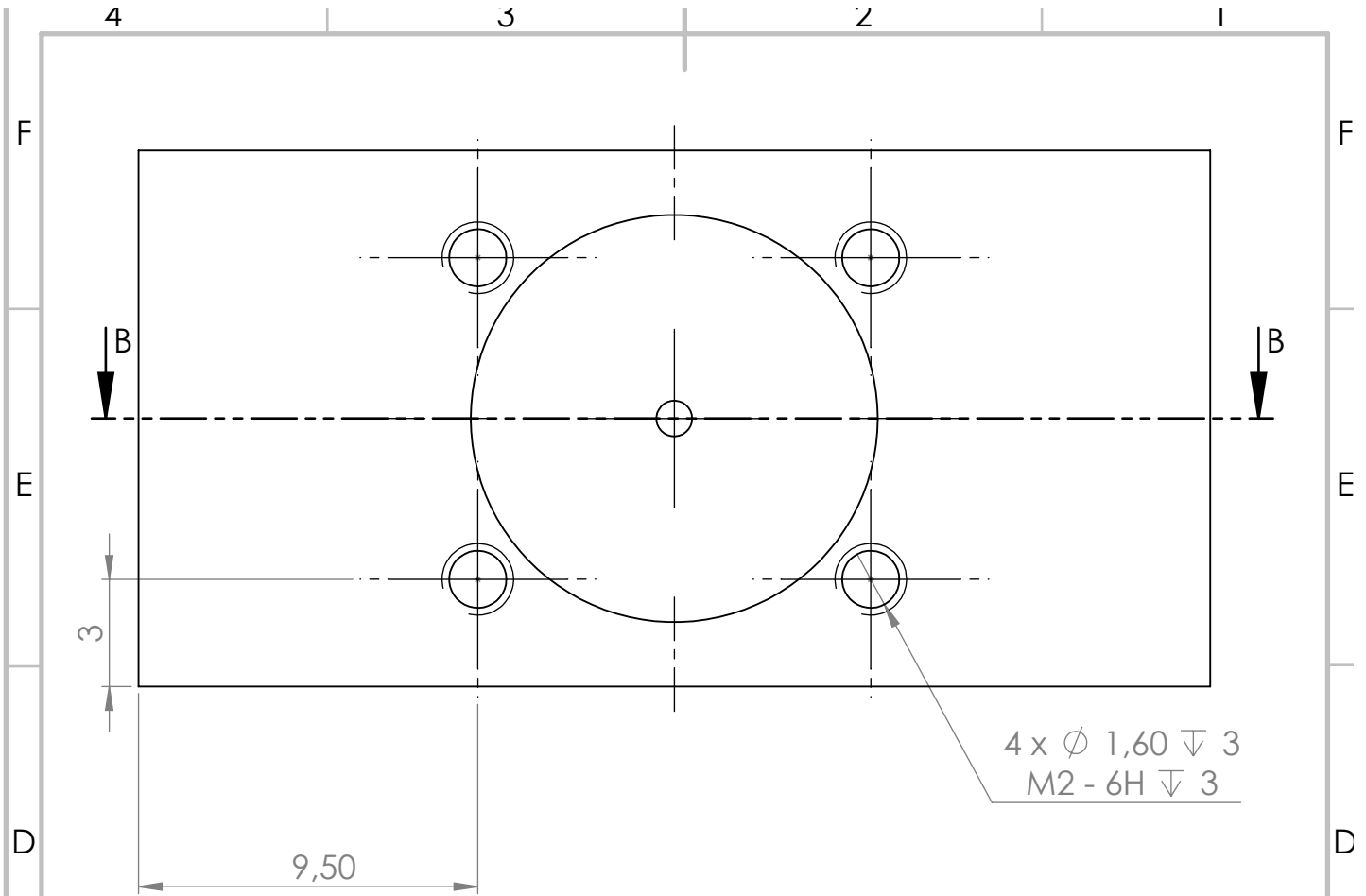
WERKSTOFF:

ZEICHNUNGSNR.

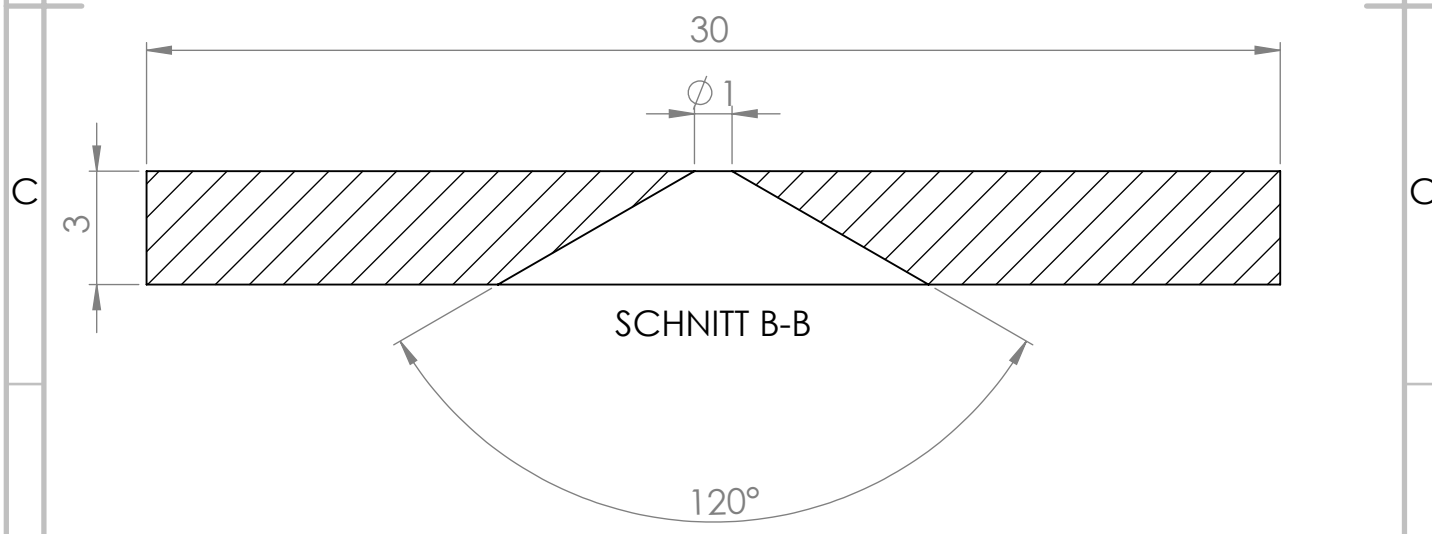
probenträger<sub>53</sub>

A4





4 x Ø 1,60 ∇ 3  
M2 - 6H ∇ 3



SCHNITT B-B

120°

WENN NICHT ANDERS DEFINIERT:  
BEMASSUNGEN SIND IN MILLIMETER  
OBERFLÄCHENBESCHAFFENHEIT:  
TOLERANZEN:  
LINEAR:  
WINKEL:

OBERFLÄCHENGÜTE:

ENTGRATEN  
UND SCHARFE  
KANTEN  
BRECHEN

ZEICHNUNG NICHT SKALIEREN

ÄNDERUNG

	NAME	SIGNATUR	DATUM		
GEZEICHNET					
GEPRÜFT					
GENEHMIGT					
PRODUKTION					
QUALITÄT					

BENENNUNG:

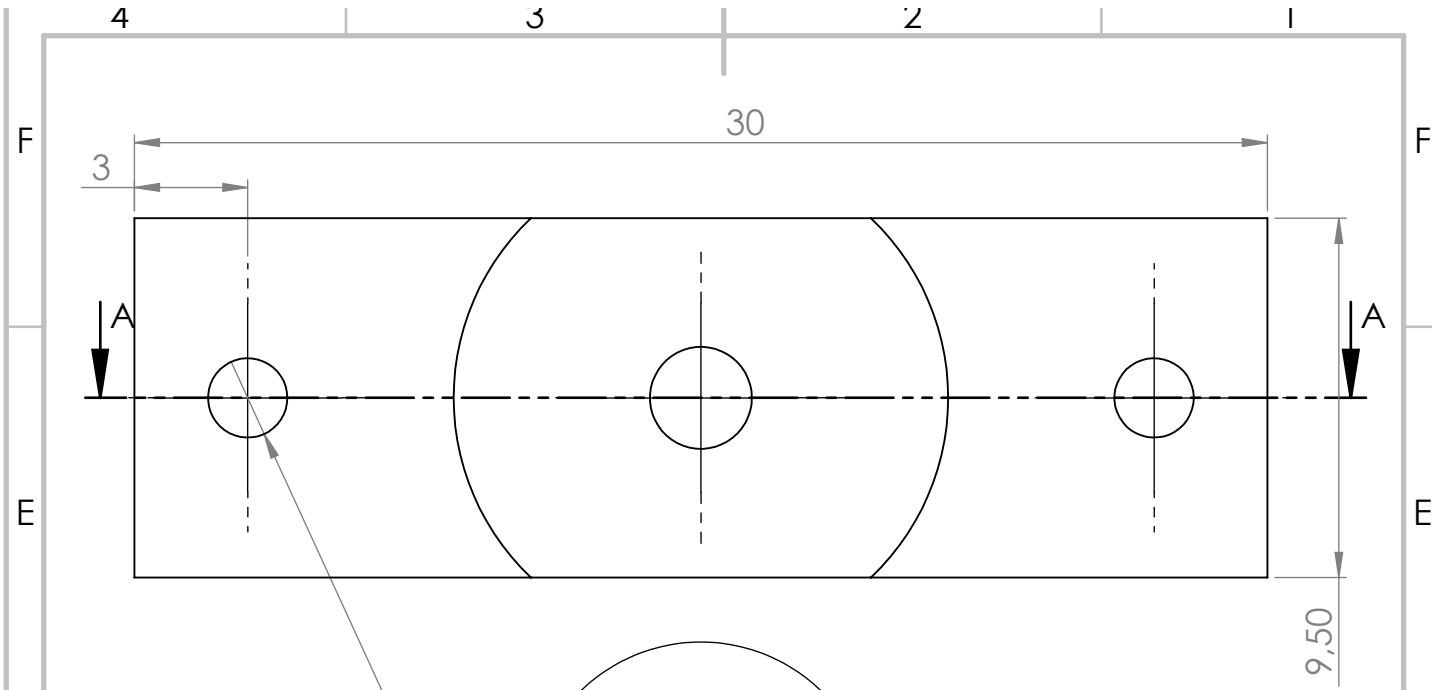
WERKSTOFF:

ZEICHNUNGSNR.

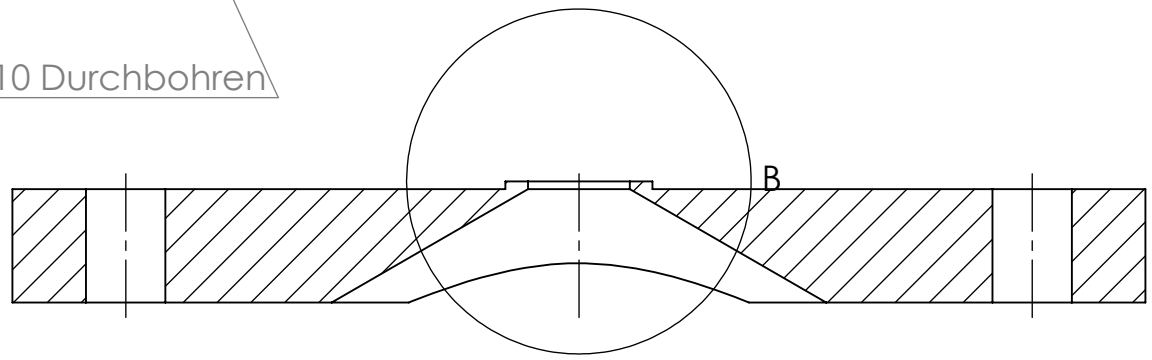
**Faraday\_cup** 55

A4

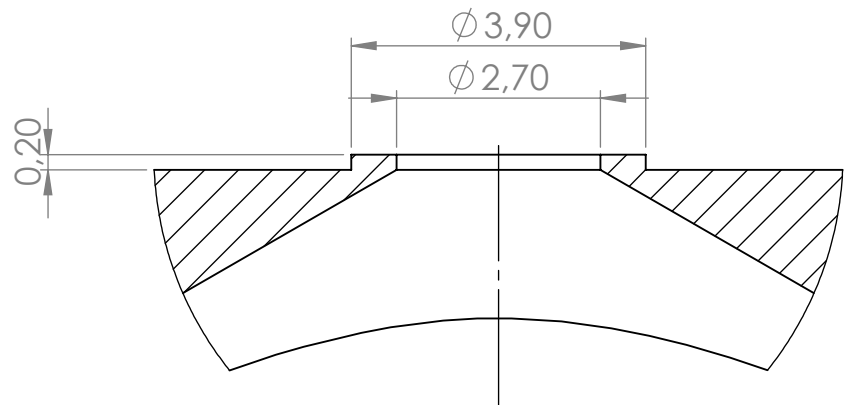




∅ 2,10 Durchbohren



SCHNITT A-A  
MAßSTAB 5 : 1



DETAIL B  
MAßSTAB 10 : 1

WENN NICHT ANDERS DEFINIERT:  
BEMASSUNGEN SIND IN MILLIMETER  
OBERFLÄCHENBESCHAFFENHEIT:  
TOLERANZEN:  
LINEAR:  
WINKEL:

OBERFLÄCHENGÜTE:

ENTGRATEN  
UND SCHARFE  
KANTEN  
BRECHEN

ZEICHNUNG NICHT SKALIEREN

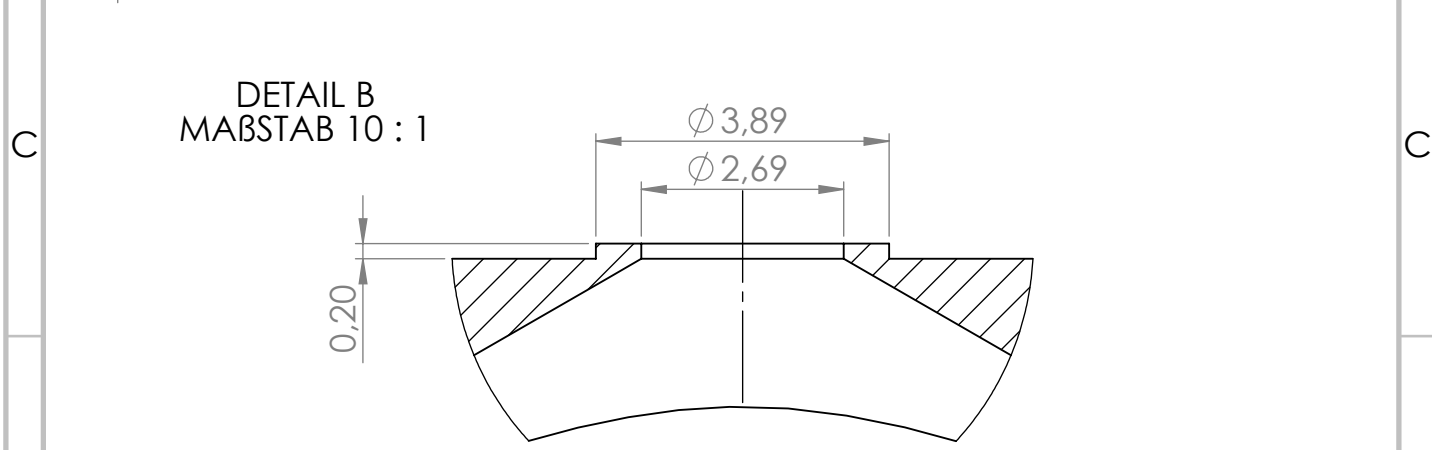
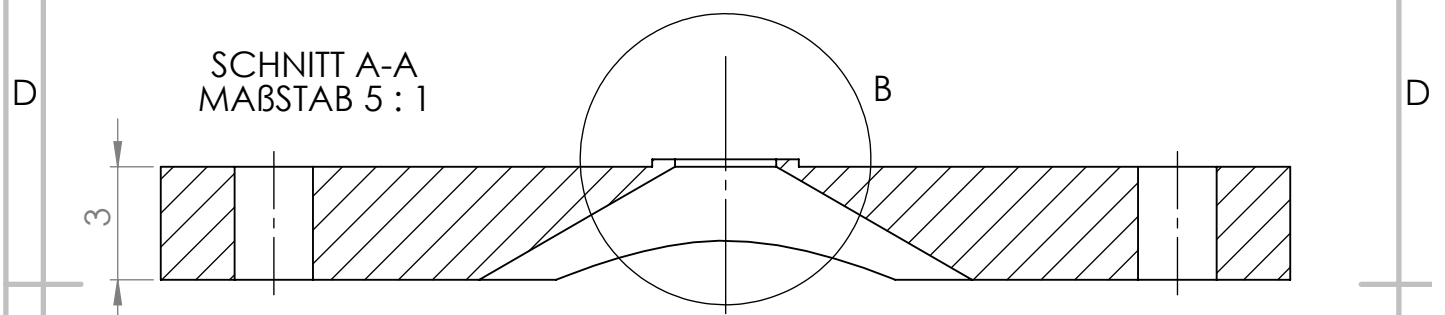
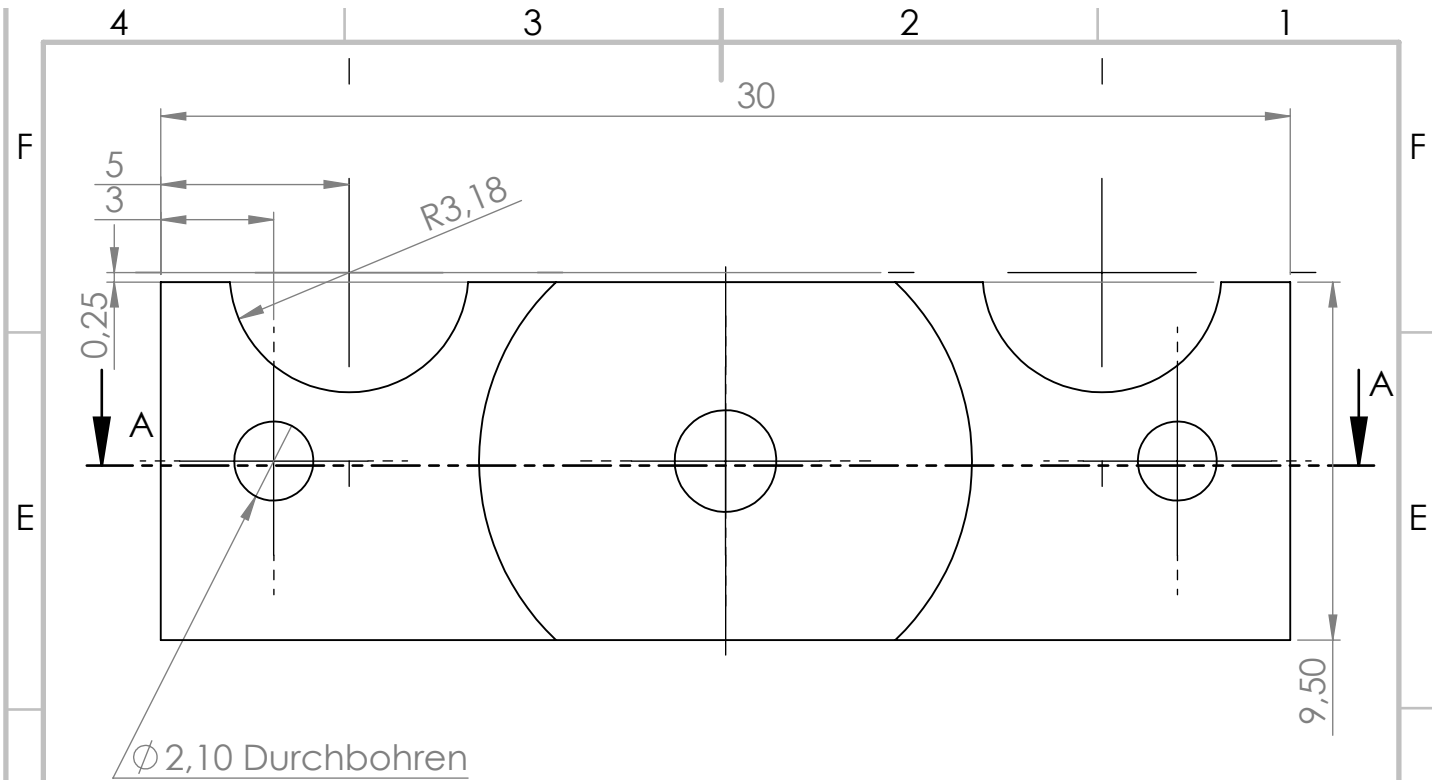
ÄNDERUNG

	NAME	SIGNATUR	DATUM		
GEZEICHNET					
GEPRÜFT					
GENEHMIGT					
PRODUKTION					
QUALITÄT					

BENENNUNG:	
WERKSTOFF:	ZEICHNUNGSNR.
	Probendruckplatte
	A4

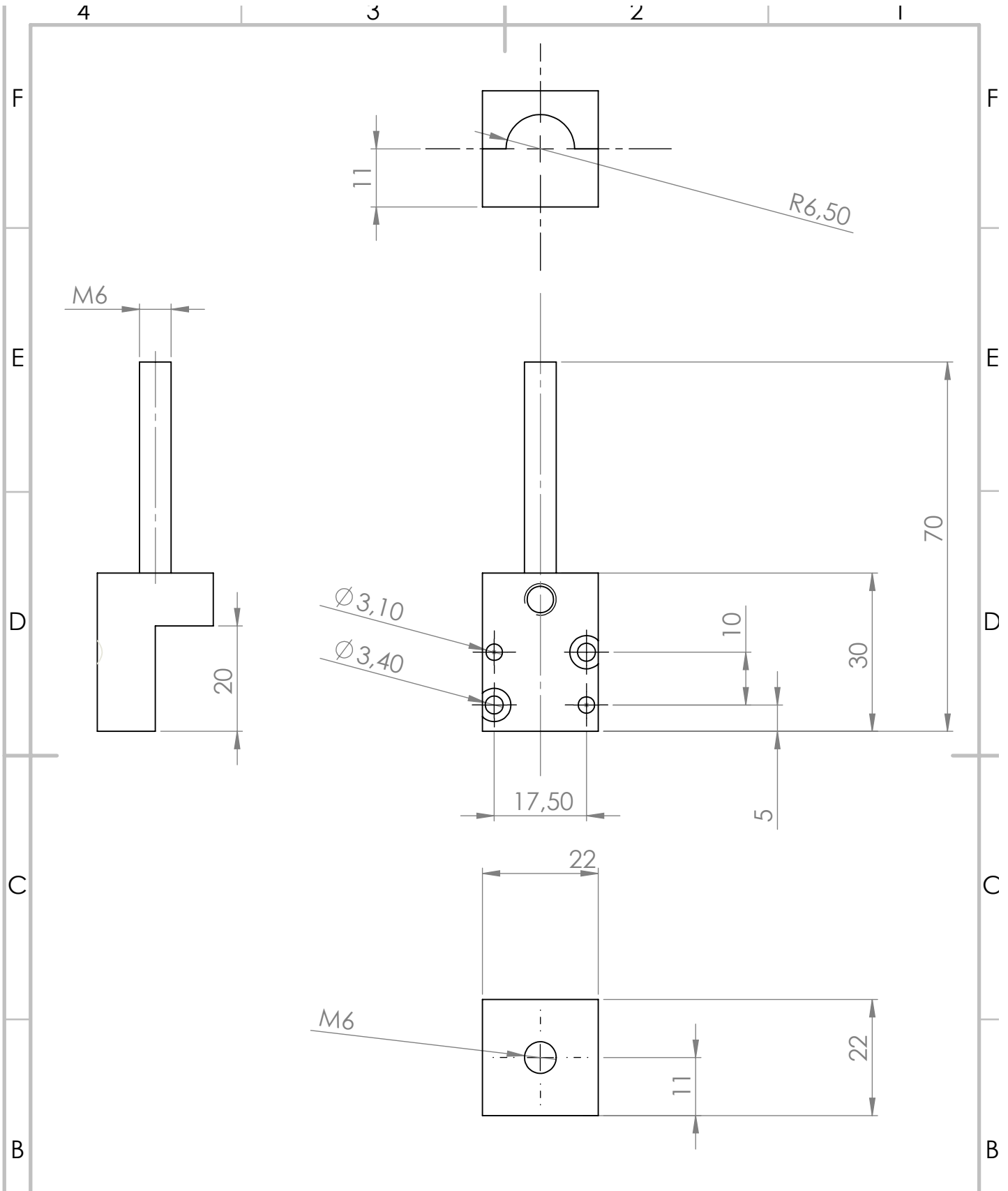






WENN NICHT ANDERS DEFINIERT: BEMASSUNGEN SIND IN MILLIMETER OBERFLÄCHENBESCHAFFENHEIT: TOLERANZEN: LINEAR: WINKEL:		OBERFLÄCHENGÜTE:		ENTGRATEN UND SCHARFE KANTEN BRECHEN		ZEICHNUNG NICHT SKALIEREN		ÄNDERUNG	
NAME		SIGNATUR		DATUM		BENENNUNG:			
GEZEICHNET									
GEPRÜFT									
GENEHMIGT									
PRODUKTION									
QUALITÄT				WERKSTOFF:		ZEICHNUNGSNR. Probendruckplatte oben			A4





WENN NICHT ANDERS DEFINIERT:  
 BEMASSUNGEN SIND IN MILLIMETER  
 OBERFLÄCHENBESCHAFFENHEIT:  
 TOLERANZEN:  
 LINEAR:  
 WINKEL:

OBERFLÄCHENGÜTE:  
 ENTGRATEN  
 UND SCHARFE  
 KANTEN  
 BRECHEN

ZEICHNUNG NICHT SKALIEREN

ÄNDERUNG

	NAME	SIGNATUR	DATUM	
GEZEICHNET				
GEPRÜFT				
GENEHMIGT				
PRODUKTION				
QUALITÄT				

BENENNUNG:

WERKSTOFF:

ZEICHNUNGSNR.  
 Lineardurchführung Teil1

A4



4

3

2

1

F

F

E

E

D

D

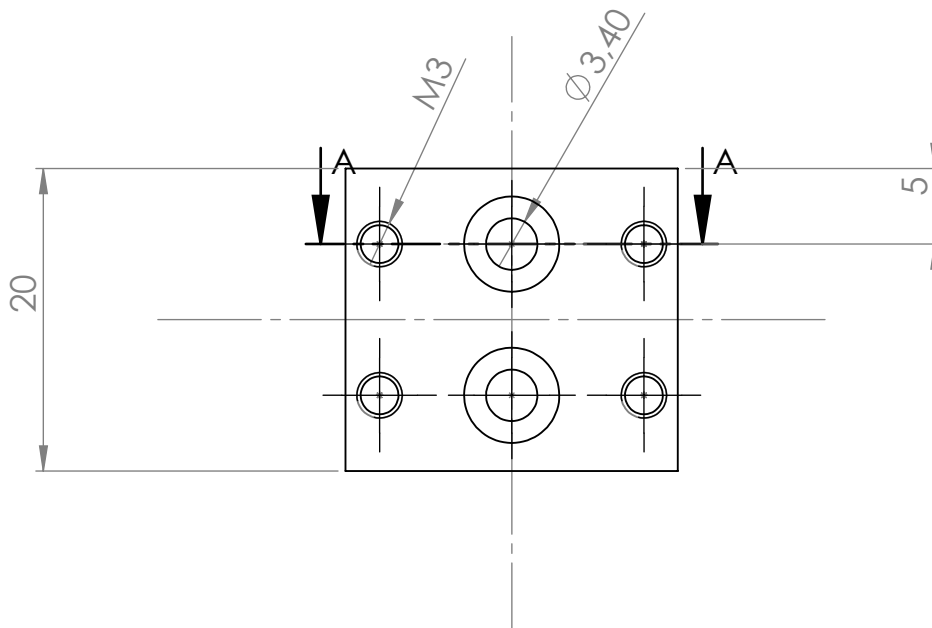
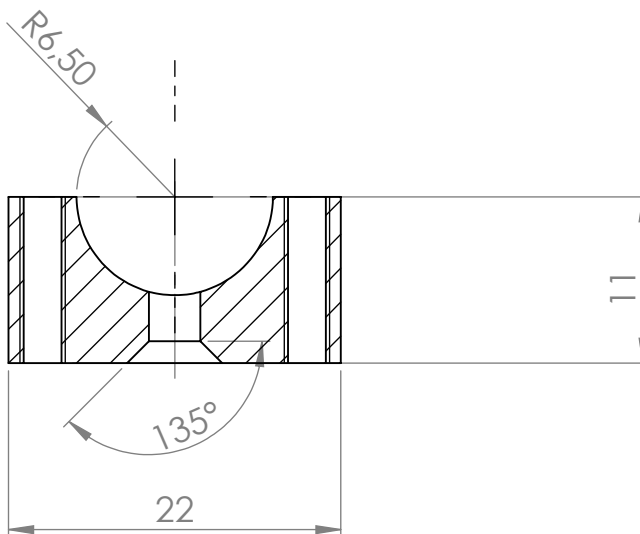
C

C

B

B

SCHNITT A-A



WENN NICHT ANDERS DEFINIERT:  
 BEMASSUNGEN SIND IN MILLIMETER  
 OBERFLÄCHENBESCHAFFENHEIT:  
 TOLERANZEN:  
 LINEAR:  
 WINKEL:

OBERFLÄCHENGÜTE:

ENTGRATEN  
 UND SCHARFE  
 KANTEN  
 BRECHEN

ZEICHNUNG NICHT SKALIEREN

ÄNDERUNG

	NAME	SIGNATUR	DATUM		
GEZEICHNET					
GEPRÜFT					
GENEHMIGT					
PRODUKTION					
QUALITÄT					

BENENNUNG:

WERKSTOFF:

ZEICHNUNGSNR.

Lineardurchführung Teil 2

A4



4

3

2

1

F

F

E

E

D

D

C

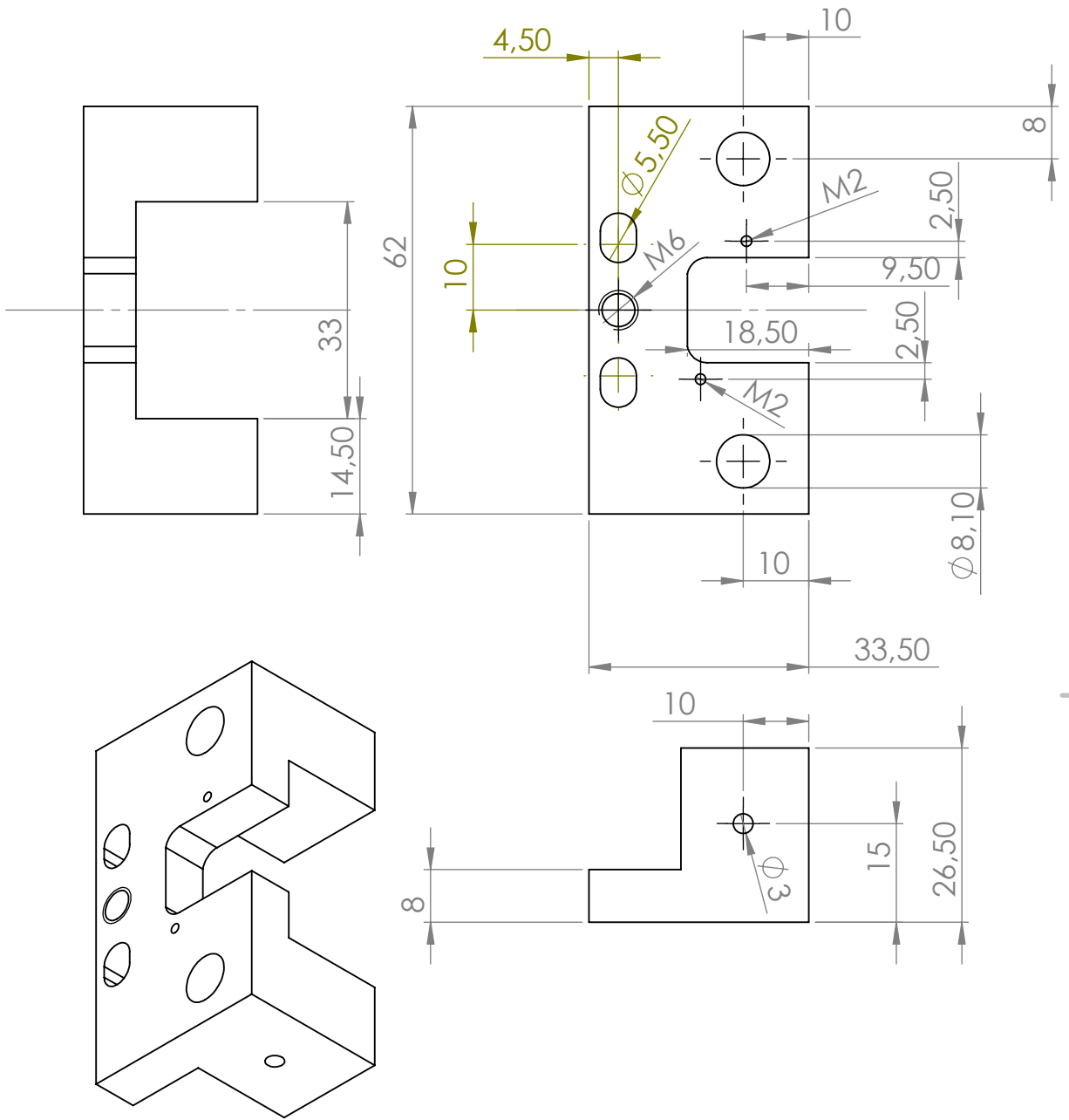
C

B

B

A

A



WENN NICHT ANDERS DEFINIERT:  
 BEMASSUNGEN SIND IN MILLIMETER  
 OBERFLÄCHENBESCHAFFENHEIT:  
 TOLERANZEN:  
 LINEAR:  
 WINKEL:

OBERFLÄCHENGÜTE:

ENTGRATEN  
 UND SCHARFE  
 KANTEN  
 BRECHEN

ZEICHNUNG NICHT SKALIEREN

ÄNDERUNG

	NAME	SIGNATUR	DATUM		
GEZEICHNET					
GEPRÜFT					
GENEHMIGT					
PRODUKTION					
QUALITÄT					

WERKSTOFF:

BENENNUNG:

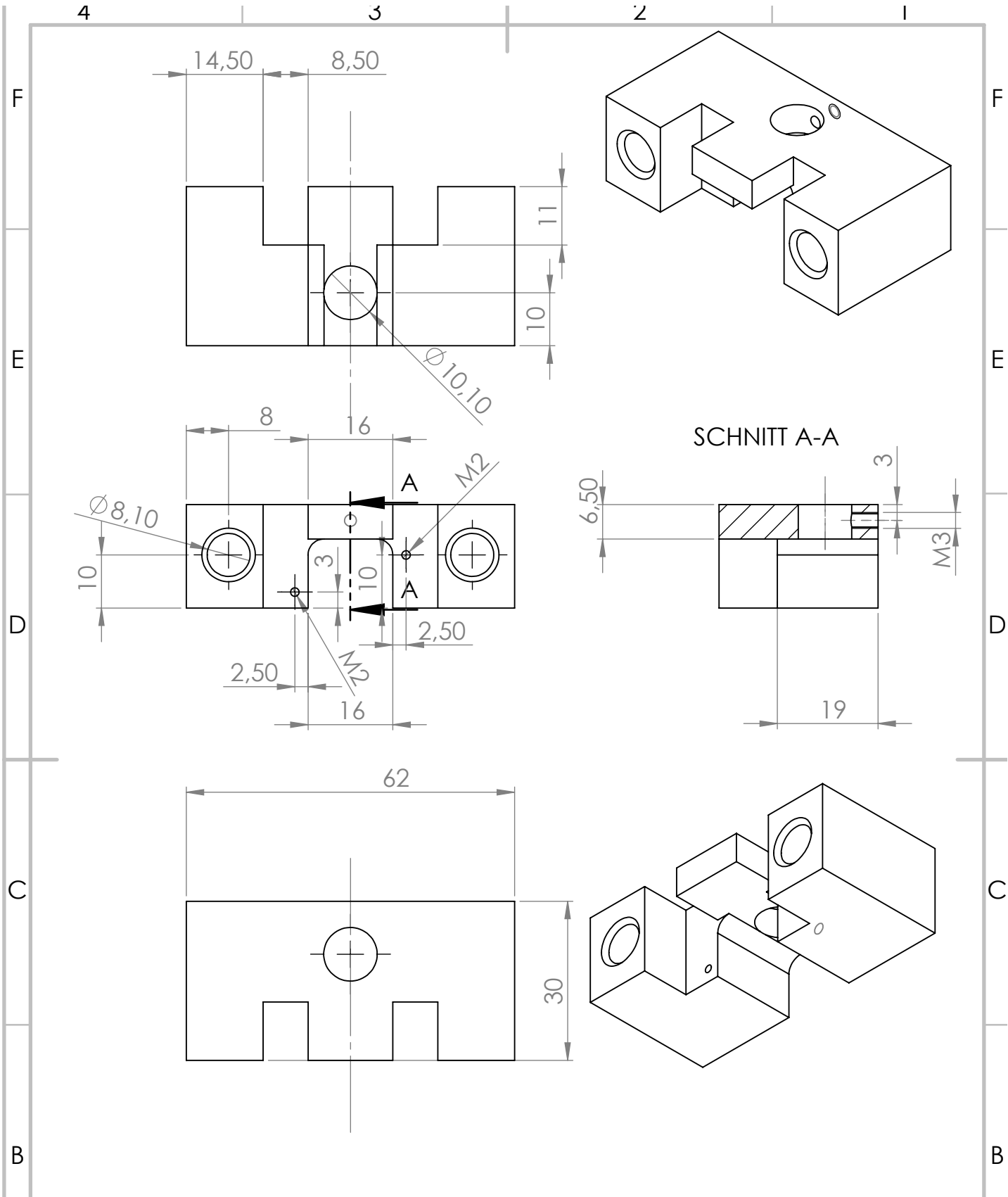
ZEICHNUNGSNR.

Targethalterträgerplatte

A4







WENN NICHT ANDERS DEFINIERT:  
 BEMASSUNGEN SIND IN MILLIMETER  
 OBERFLÄCHENBESCHAFFENHEIT:  
 TOLERANZEN:  
 LINEAR:  
 WINKEL:

OBERFLÄCHENGÜTE:  
  
 ENTGRATEN  
 UND SCHARFE  
 KANTEN  
 BRECHEN

ZEICHNUNG NICHT SKALIEREN  
 ÄNDERUNG

	NAME	SIGNATUR	DATUM		
GEZEICHNET					
GEPRÜFT					
GENEHMIGT					
PRODUKTION					
QUALITÄT					

BENENNUNG:  
  
 ZEICHNUNGSNR.  
**Targethalterankerplatte**  
 A4



4

3

2

1

F

F

E

E

D

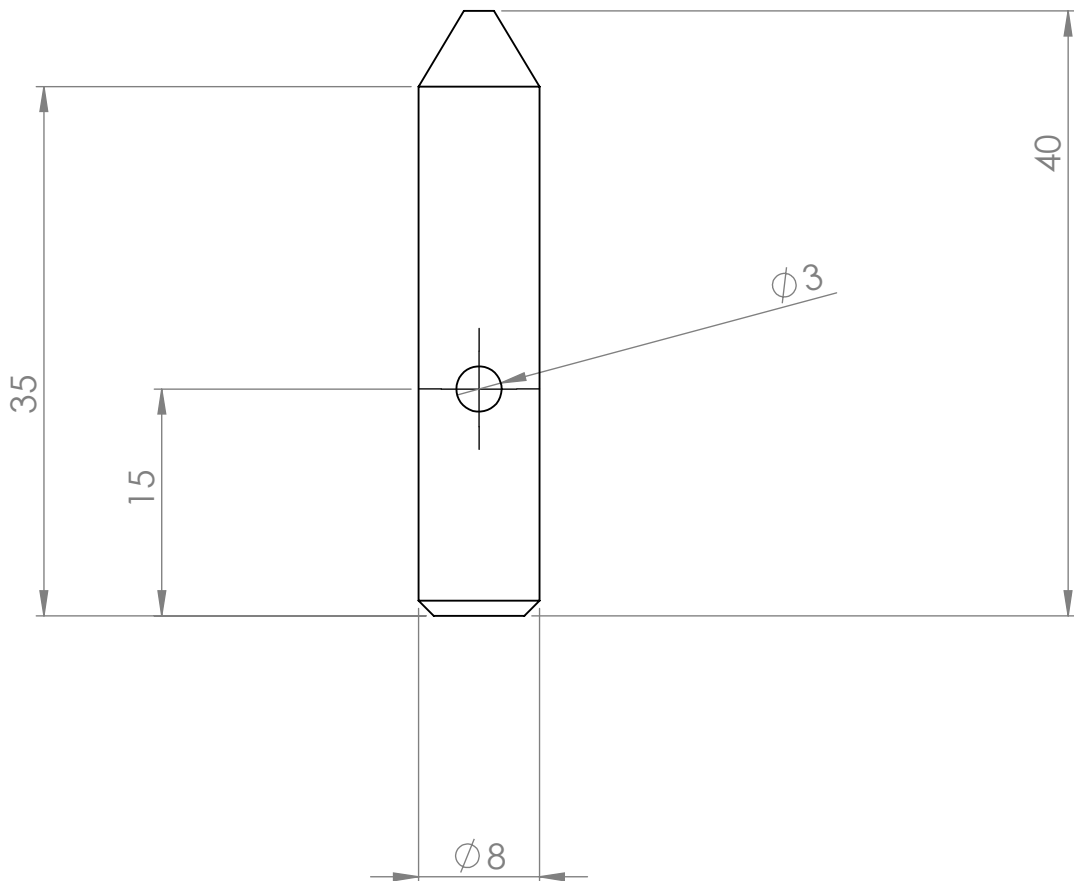
D

C

C

B

B



WENN NICHT ANDERS DEFINIERT:  
 BEMASSUNGEN SIND IN MILLIMETER  
 OBERFLÄCHENBESCHAFFENHEIT:  
 TOLERANZEN:  
 LINEAR:  
 WINKEL:

OBERFLÄCHENGÜTE:

ENTGRATEN  
 UND SCHARFE  
 KANTEN  
 BRECHEN

ZEICHNUNG NICHT SKALIEREN

ÄNDERUNG

	NAME	SIGNATUR	DATUM		
GEZEICHNET					
GEPRÜFT					
GENEHMIGT					
PRODUKTION					
QUALITÄT					

BENENNUNG:

WERKSTOFF:

ZEICHNUNGSNR.  
 Verbindungsstift

A4



4

3

2

1

F

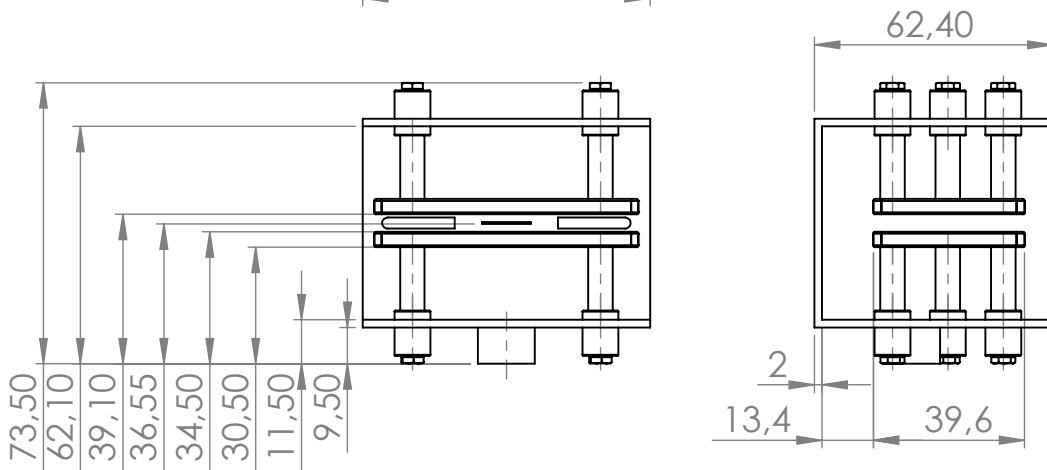
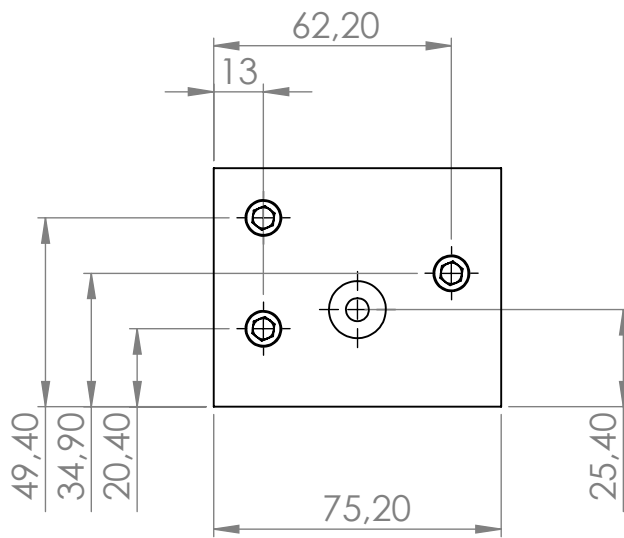
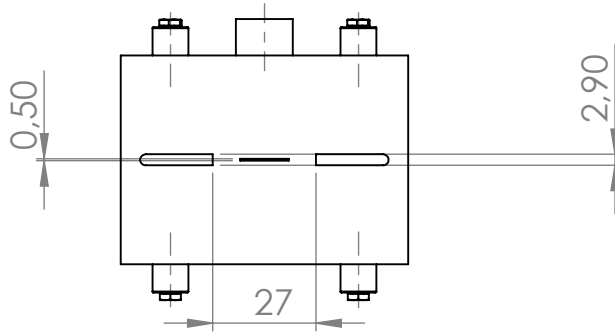
E

D

C

B

A



WENN NICHT ANDERS DEFINIERT:  
BEMASSUNGEN SIND IN MILLIMETER  
OBERFLÄCHENBESCHAFFENHEIT:  
TOLERANZEN:  
LINEAR:  
WINKEL:

OBERFLÄCHENGÜTE:

ENTGRATEN  
UND SCHARFE  
KANTEN  
BRECHEN

ZEICHNUNG NICHT SKALIEREN

ÄNDERUNG

	NAME	SIGNATUR	DATUM
GEZEICHNET			
GEPRÜFT			
GENEHMIGT			
PRODUKTION			
QUALITÄT			

WERKSTOFF:

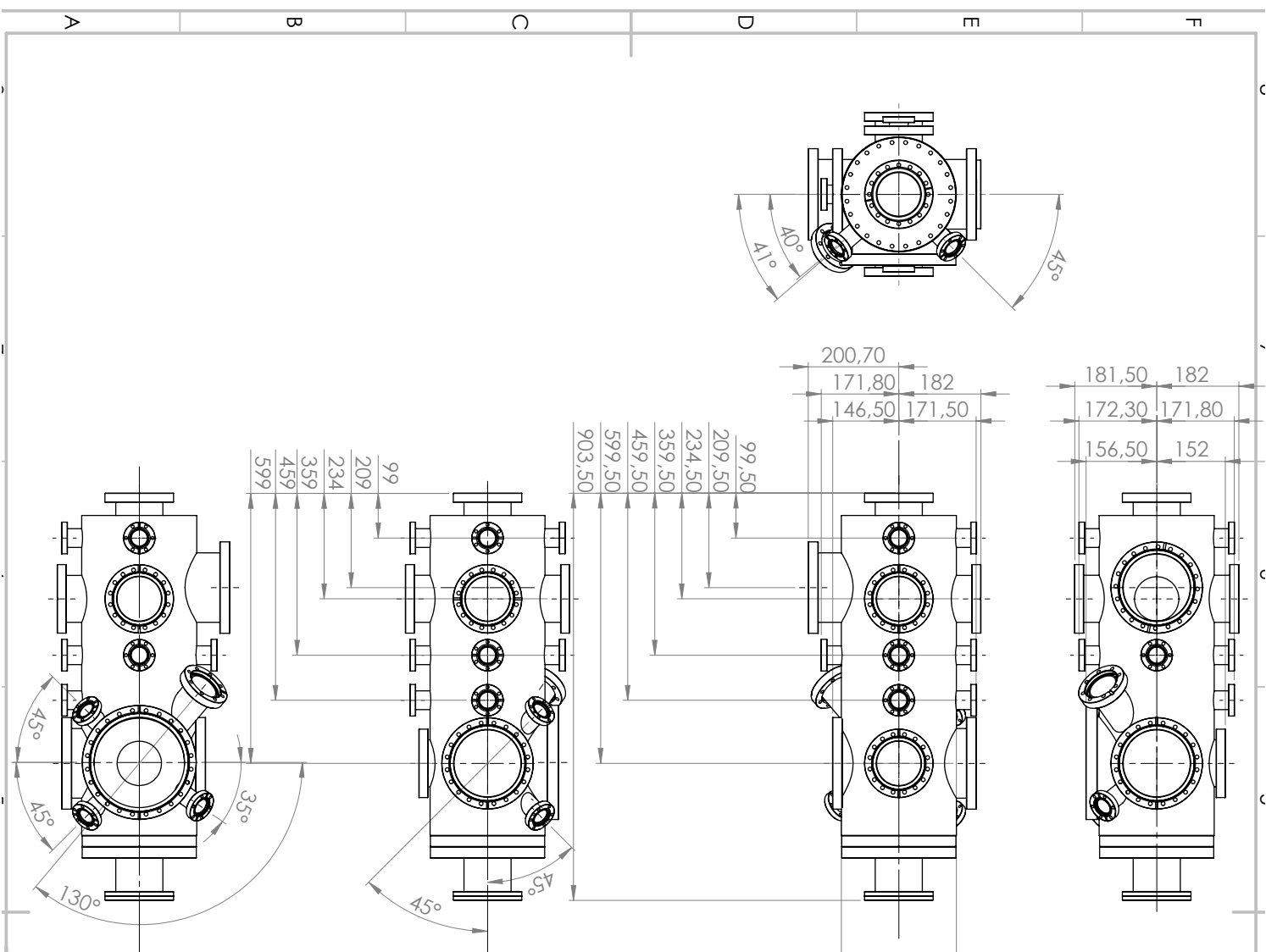
BENENNUNG:

ZEICHNUNGSNR.

chopper all 71

A4



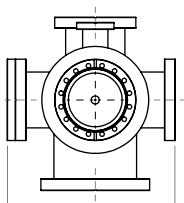
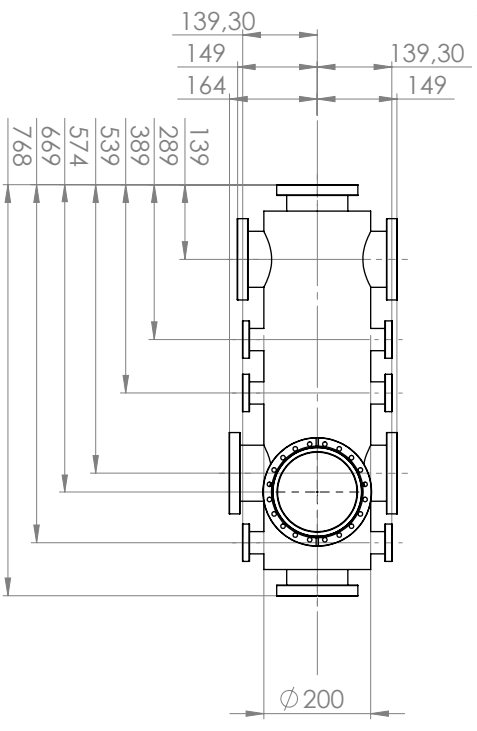
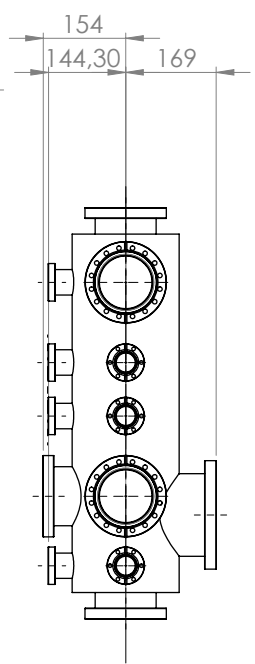
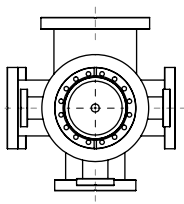


WENN NICHT ANDERS DEFINIERT: BEWÄSSERUNGEN SIND IN MILLIMETER OBERFLÄCHENRÜHRSCHAFTENRUH: TOLERANZEN: LINIEN: WINKEL:		OBERFLÄCHENRÜHRSCHAFTENRUH: RÜHRSCHAFTEN KANTEN RÜHRSCHAFTEN		ZEICHNUNG NICHT SKALIEREN		ÄNDERUNG:	
NAMEN	SIGNATUR	DATUM					
GEZEICHNET							
GEPRÜFT							
GENEHMIGT							
PRODUCTION							
QUALITÄT							
WERKSTOFF:				ZEICHNUNGSNR.			
GEBÜCHT:				MASSSTAB: 1:10			
<b>Zusammenbau Targetkar</b>							
BLATT 1 VON 1							

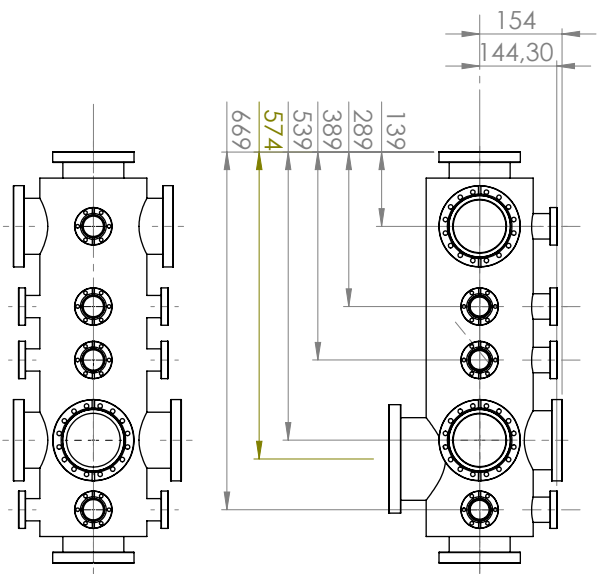




A B C D E F



313



WENN NICHT ANDERS DENIERT: BEWASSUNGEN SIND IN MILLIMETER OBERFLÄCHENBESCHAFFENHEIT: TOLERANZEN: LUNGEN: WINKEL:			OBERFLÄCHENGÜTE:     RINGKANTEN UND SCHÄRFE KANTEN BRECHEN			ZEICHNUNG NICHT SKALIEREN     ÄNDERUNG			
GERICHNET	NAME	SIGNATUR	DATUM	BRÜNNUNG:			ZEICHNUNGSNR.		
GERÜFT				WERKSTOFF:			Zusammenbau_T01		
GENEHMIGT				GERWICHT:			MASSSTAB:1:10		
PRODUKTION				QUALITÄT:			BLATT 1 VON 1		